Astronomy & Astrophysics manuscript no. draft
January 28, 2025 ©ESO 2025

Numerical Study of Solar Eruption, EUV Wave Propagation, and Wave-Induced Prominence Dynamics

V. Liakh[1] and R. Keppens[2]

[1] Rosseland Centre for Solar Physics, University of Oslo, PO Box 1029, Blindern 0315, Oslo, Norway e-mail: `valeriia.liakh@astro.uio.no`
[2] Centre for mathematical Plasma Astrophysics, Department of Mathematics, KU Leuven, Celestijnenlaan 200B, 3001 Leuven, Belgium

arXiv:2501.15697v1 [astro-ph.SR] 26 Jan 2025

ABSTRACT

Context. Extreme Ultraviolet (EUV) waves, frequently produced by eruptions, propagate through the non-uniform magnetic field of the solar corona and interact with distant prominences, inducing their global oscillations. However, the generation, propagation, and interaction of these waves with distant prominences remain poorly understood.

Aims. We aim to study the influence of an eruptive flux rope (EFR) on a distant prominence by means of extreme-resolution numerical simulations. We cover a domain of horizontal extent of 1100 Mm while capturing details down to 130 km using automated grid refinement.

Methods. We performed a 2.5D numerical experiment using the open-source `MPI-AMRVAC 3.1` code, modeling an eruption as a 2.5D catastrophe scenario augmented with a distant dipole magnetic field to form the flux rope prominence.

Results. Our findings reveal that the EFR becomes unstable and generates a quasicircular front. The primary front produces a slow secondary front when crossing equipartition lines where the Alfvén speed is close to the sound speed. The resulting fast and slow EUV waves show different behaviors, with the fast EUV wave slightly decelerating as it propagates through the corona, while the slow EUV wave forms a stationary front. The fast EUV wave interacts with the remote prominence, driving both transverse and longitudinal oscillations. Additionally, magnetic reconnection at a null point below the prominence flux rope is triggered by the fast EUV wave, affecting the flux rope magnetic field and the prominence oscillations.

Conclusions. Our study unifies important results of the dynamics of eruptive events and their interactions with distant prominences, including details of (oscillatory) reconnection and chaotic plasmoid dynamics. We demonstrate for the first time the full consequences of remote eruptions on prominence dynamics and clarify the damping mechanisms of prominence oscillations.

Key words. Sun: corona – Sun: filaments, prominences – Sun: oscillations – methods: numerical

1. Introduction

Solar prominences are cool, dense plasma clouds typically located in magnetic dips high in the solar corona, where they are supported against gravity by magnetic forces. These structures are highly dynamic, one manifestation of this dynamism is prominence oscillations. Such oscillations are generally classified as small-amplitude (SAOs) or large-amplitude oscillations (LAOs), based on their velocities, with a threshold of 10 km/s (see reviews by Oliver & Ballester 2002; Arregui et al. 2018). Additionally, prominence oscillations are classified by the direction of plasma motion relative to the magnetic field as longitudinal and transverse, respectively. Further details on the classification and characteristics of these oscillations can be found in the latest update of the living review by Arregui et al. (2018).

Large-amplitude oscillations are expected to contain significant energy due to the large mass and velocities associated with prominences. Most observed LAO events have been linked to energetic disturbances. Numerous studies have reported LAO excitation in filaments induced by Moreton and Extreme Ultraviolet (EUV) waves (Gilbert et al. 2008; Asai et al. 2012; Liu et al. 2013; Shen et al. 2014; Xue et al. 2014; Takahashi et al. 2015; Shen et al. 2017; Pant et al. 2016; Wang et al. 2016; Zhang et al. 2017; Mazumder et al. 2020). Simultaneous excitation of different LAO polarizations (with the polarization identified by the direction of plasma motions) from a single energetic event has also been observed. For example, Gilbert et al. (2008) reported an instance in which filament oscillations induced by a Moreton wave exhibited mixed polarization modes. Recently, studies by Devi et al. (2022), Zhang et al. (2024b), and Zhang et al. (2024a) reported EUV waves from eruption events exciting prominence oscillations. However, the specific mechanisms underlying the generation, propagation, and substantial energy transfer from these disturbances to prominences, which trigger LAOs, remain unclear.

Early evidence of such waves was reported by Moreton & Ramsey (1960), who observed waves emanating from flares or coronal mass ejections (CMEs) and propagating through the solar atmosphere at velocities ranging from 500 – 1500 km/s. The Moreton wave is widely recognized as a fast-mode wave propagating through the chromosphere and low corona. The EUV Imaging Telescope (EIT) aboard the Solar and Heliospheric Observatory (SOHO) detected another wave-like phenomenon in the solar corona, named after the telescope as the EIT wave (Moses et al. 1997; Thompson et al. 1998). These EIT waves propagate at speeds of 200 – 300 km/s and are typically associated with CMEs or eruptions (Biesecker et al. 2002; Chen 2006, 2011). Initially, EIT waves were considered the coronal counterparts of Moreton waves (Thompson et al. 1998; Wang 2000). However, this interpretation was challenged by the observed velocities of EIT waves, which are typically about three times lower than those of Moreton waves. Moreover, observations revealed that EIT fronts can become stationary, being trapped in magnetic arcades, decelerating and eventually halting near quasi-separatrix layers (QSL) (Delannée & Aulanier 1999; DeVore & Antiochos 2000). Since fast-mode waves are expected to propagate through QSLs, this behavior implies that EIT waves have a distinct physical nature. Several theories have been proposed to explain EIT waves, including the magnetic field line stretching model (Chen et al. 2002, 2005), the successive reconnection model (Attrill et al. 2007), the slow-mode wave model (Wills-Davey et al. 2007), and the current shell model (Delannée et al. 2008).

The launch of the Solar Dynamics Observatory (SDO) with its Atmospheric Imaging Assembly (AIA) marked a new era in observing these phenomena. The EIT waves began to be predominantly referred to as EUV waves due to their detection in the extreme ultraviolet range. Observations with SDO/AIA have provided significant insights into these phenomena. However, the uncertainty regarding the physical nature of EUV waves persisted. On the one hand, Liu et al. (2010), Chen & Wu (2011a), Chen & Wu (2011b), and Zheng et al. (2013) identified both fast EUV waves and non-wave-like slow EUV phenomena, supporting the magnetic field stretching model. On the other hand, many observations of the interactions of the EUV waves with the different magnetic objects in the solar corona suggested the fast magnetoacoustic wave nature of EUV phenomena. For instance, Olmedo et al. (2012) observed the interaction of an EUV wave with a coronal hole, which resulted in refraction, reflection, and transmission. The EUV wave reflection from a coronal hole was detected in many observations (see, e.g., Long et al. 2008; Gopalswamy et al. 2009; Kienreich et al. 2013; Yang et al. 2013). Zhou et al. (2024) reported the detection of magnetohydrodynamic wave lensing in the highly ionized and magnetized coronal plasma, using observations from the SDO. In this observation, the quasi-periodic wavefronts generated by a flare converge at a specific point after traversing a coronal hole, resembling the lensing of electromagnetic waves from a source to a focal point. This magnetohydrodynamic wave lensing has been accurately reproduced in a numerical simulation. Intriguingly, Chandra et al. (2016) observed a fast EUV wave, creating a slow EUV wave near a QSL. This slow EUV wave decelerates and becomes stationary. These observations suggest that fast EUV phenomena are likely fast magnetoacoustic waves, acting as the coronal counterparts to Moreton waves. They are often initiated by eruptions and propagate through the non-uniformly magnetized solar corona. The slow EUV phenomena are best explained as slow magnetoacoustic waves or from the progressive stretching and opening of magnetic field lines during an eruption.

Numerous attempts have been made to model Moreton, EUV, and EIT waves using 2D and 3D numerical simulations. Chen et al. (2002, 2005) performed simulations of erupting flux ropes and studied the origins of Moreton and EIT waves. Their results revealed a piston-like shock surrounding the flux rope, with its skirt sweeping the solar surface at speeds exceeding 700 km/s. This shock skirt was identified as the coronal Moreton wave. Additionally, they observed a slower wave-like phenomenon propagating at approximately 200 km/s, which was attributed to an EIT wave formed by the progressive stretching and opening of magnetic field lines around the erupting flux rope. In these simulations, an enhanced density region developed ahead of the stretching field lines, forming the EIT wave, while dimmings appeared in the inner region behind it.

Using a 2.5D catastrophic scenario, Wang et al. (2009) and Wang et al. (2015) identified a fast magnetoacoustic wave interpreted as a fast EUV wave, as well as slow magnetoacoustic wave fronts, echoes, and vortices, which were suggested to correspond to slow EUV waves. Mei et al. (2012) showed that stronger background fields and lower densities produce more energetic waves. An intriguing feature in their study was the detection of secondary echoes, where the interaction between echoes, slow fronts, and vortices resembled earlier findings by Wang et al. (2009). Using a 3D model, Mei et al. (2020) confirmed the presence of fast and slow shocks produced by eruption, echoes, and vortices, noting the difficulty of slow shock front detection in synthetic EUV images compared to fast shock fronts.

Similarly, data-driven simulations have been employed to reproduce coronal wave dynamics (Cohen et al. 2009; Downs et al. 2011, 2012, 2021). Cohen et al. (2009) simulated diffuse bright fronts observed by STEREO/EUVI and distinguished between wave-like and non-wave EUV phenomena. Downs et al. (2011, 2012) detected a fast magnetoacoustic front in their experiments, which became detached from the eruption, and a compression front directly linked to the eruption itself.

Chen et al. (2016) explored the formation of stationary fronts after a passage of the primary front through QSLs. They concluded that fast-to-slow mode conversion at the QSL results in a slow front that stops at the next separatrix, forming a stationary front. Downs et al. (2021) further highlighted the potential of studying fast EUV wave kinematics as a diagnostic tool for probing the coronal medium.

From a theoretical perspective, the interaction of Moreton and EUV waves with surrounding magnetic arcades, coronal holes, and prominences has been extensively studied (see, e.g., Piantschitsch et al. 2017; Afanasyev & Zhukov 2018; Liakh et al. 2020; Zurbriggen et al. 2021; Liakh et al. 2023; Piantschitsch et al. 2023, 2024). Liakh et al. (2020) simulated wave triggering using an artificial perturbation to mimic an energetic disturbance, such as a distant flare, located at a certain distance from the prominences. Building on this, Liakh et al. (2023) employed a more advanced model to study the self-consistent triggering of a nearby prominence caused by the eruption. In this scenario, the triggering mechanism was primarily due to the evolution of plasmoids in the current sheet. Despite the important results obtained from both observational and numerical studies, significant gaps remain in our understanding of EUV wave formation, the propagation in a non-uniformly magnetized coronal medium, and the interaction of these perturbations with distant prominences. In this paper, we comprehensively study all these aspects using a 2.5D numerical model.

This paper is organized as follows: In Section 2, we describe the numerical setup of the experiment. In Section 3, we present the main results, describing the different stages of the numerical experiment, including the onset of the eruption, the propagation of the front, its interaction with the prominence, and the response of the prominence to the perturbation. Lastly, in Sections 4 and 5, we discuss and summarize the main findings.

2. Numerical setup

The numerical experiment is performed using the fully open-source, adaptive-grid, parallelized Adaptive Mesh Refinement Versatile Advection Code (`MPI-AMRVAC 3.1`)[1] (Porth et al. 2014; Xia et al. 2018; Keppens et al. 2021; Keppens et al. 2023). We use a Cartesian coordinate system, with the x- and y-axes denoting the horizontal and vertical directions, respectively. The numerical domain has a physical size of 1100×500 Mm and

[1] `MPI-AMRVAC 3.1`, available at http://amrvac.org.

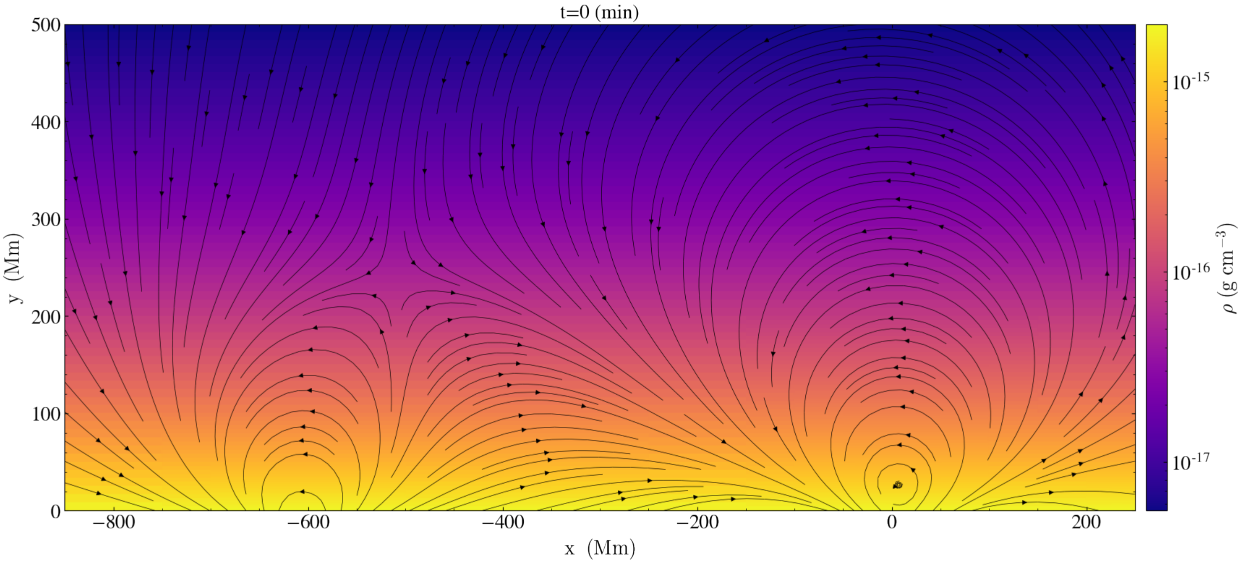

Fig. 1: Initial density distribution and magnetic field lines in the entire numerical domain. Animation 1 shows the global evolution of the density, temperature, $v_{\parallel} = (\mathbf{v} \cdot \mathbf{B})/B$ and $v_{\perp} = v_y - v_{\parallel} B_y/B$ during the entire simulation time. (An animation of this figure is available online.)

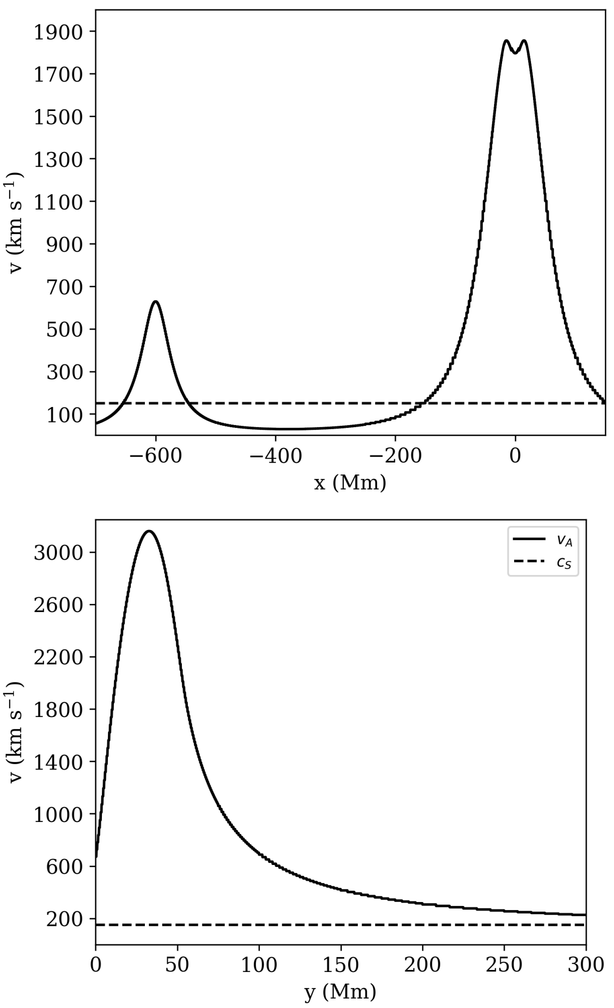

Fig. 2: Alfvén and sound speed along the horizontal cut at $y = 10$ Mm (top) and the vertical cut at $x = 0$ Mm (bottom).

consists of 132×60 grid cells at the base resolution. To achieve higher resolution, where needed, we apply seven levels of AMR, resolving structures down to the smallest grid cell size of 130.2 km. This resolution is comparable to that of previous 2.5D numerical studies on wave-induced prominence dynamics (Liakh et al. 2020; Zurbriggen et al. 2021; Liakh et al. 2023). The AMR employs a Lohner-type prescription (Lohner 1987), using second-order gradient evaluations of both density and magnetic field components. Additionally, the base resolution is enforced in three specific regions near the top and side boundaries: $x < -750$ Mm, $x > 50$ Mm starting at $t = 5.7$ minutes, and $y > 300$ Mm throughout the entire numerical experiment.

The `MPI-AMRVAC 3.1` code solves MHD equations that include non-ideal, non-adiabatic, and various physical source terms like the solar gravitational field. The MHD equations can be found in textbooks (e.g. Goedbloed et al. 2019) and are equivalent to Eqs. (2-5) as presented in Brughmans et al. (2022). For the equation of state, we use the ideal gas law for a monoatomic gas with a specific heat ratio $\gamma = 5/3$. The mean molecular mass is $\mu \approx 0.6$, since we assume fully-ionized plasma with the Helium abundance $n_{He} = 0.1 n_H$. The energy equation contains terms of optically thin radiation, anisotropic thermal conduction, and Ohmic heating due to a numerical magnetic resistivity. The energy balance equation also includes a fixed background heating term in the form of exponential decay to compensate initially for radiative losses.

The set of MHD equations is solved using the Harten–Lax–van Leer flux scheme (HLL) (Harten et al. 1983) with the second-order symmetric Total Variation Diminishing (TVD) slope limiter (van Leer 1974). The time integration is performed using the Runge-Kutta three-step method. To ensure the $\nabla \cdot \mathbf{B} = 0$ condition, the parabolic diffusion method is applied (Keppens et al. 2003, 2023). For the thin radiative losses, we use the Colgan-DM cooling curve from Colgan et al. (2008), extended with a low-temperature treatment using 12,000 points to resolve the temperature in an interpolated table (for details see Hermans & Keppens 2021). The optically thin radiative losses are added using the exact integration scheme from Townsend (2009).

The initial atmosphere is a gravitationally stratified corona assuming the constant temperature $T_0 = 1$ MK and the gravitational acceleration defined as $g(y) = g_\odot R_\odot^2/(R_\odot + y)^2$, where $g_\odot = 2.74 \times 10^4 \mathrm{cm\,s^{-2}}$ is the gravitational acceleration at the solar surface and $R_\odot = 696.1$ Mm is the solar radius. The pressure scale height then varies along the vertical direction as $H(y) = H_0(R_\odot + y)/R_\odot$, where $H_0 \approx 50$ Mm is the pressure scale height at the bottom. The pressure, density and background heating have the following values at $y = 0$: $p_{0,bot} = 0.298$ dyn cm^{-2}, $\rho_{0,bot} = 2 \times 10^{-15}$ g cm^{-3}, and $\mathcal{H}_b(y) = \rho_0^2 \Lambda(T_0) e^{-2y/H(y)} = 3.972 \times 10^{-4}$ ergs cm^{-3} s^{-1}. We include anisotropic thermal conduction $\nabla \cdot (\overleftrightarrow{\kappa} \cdot \nabla T)$ along the magnetic field lines, using the Spitzer conductivity $\kappa_\parallel = 8 \times 10^{-7}\, T^{5/2}$ ergs cm^{-1}s^{-1}K^{-1} (Spitzer 2006). In this experiment, $\kappa_\perp$ is neglected due to its comparably small value compared to $\kappa_\parallel$. In order to add the parabolic source term of the anisotropic thermal conduction, we use the Runge-Kutta Legendre super-time-stepping technique (RKL; Meyer et al. 2014).

Figure 1 presents the magnetic configuration, which consists of the 2.5D catastrophic magnetic field described by Takahashi et al. (2017) and a dipolar magnetic field. The 2.5D catastrophic magnetic field consists of a cylindrical current, an image current beneath the lower boundary to produce an upward magnetic force, and a background quadrupolar magnetic field producing a balancing downward magnetic force and has various parameters setting the rope center and magnetic field strength. Then, the eruption occurs when the parameter of the strength of the quadrupolar field is $M_q < 27/8$. We set $M_q = 0.8 \times 27/8$ in our configuration in order to obtain an immediate eruption. The eruptive flux rope (EFR) is centered at $X = 0$ and $Y = 27$ Mm, with a radius of $R = 27$ Mm and the magnetic field strength at the center, $B = 36.6$ G. The 2.5D catastrophe model is chosen because it offers a straightforward and effective method for producing eruptions within a 2.5D numerical setup. The dipolar magnetic field is centered at $X = -600$ Mm (see Fig. 1). The dipole is placed at the depth $h_d = 20$ Mm and provides the magnetic field strength at the bottom of the numerical domain at $x = -600$ Mm, set to $B = 18.9$ G.

Since the global configuration consists of the superposition of the 2.5D catastrophe and an ordinary dipolar field, the global magnetic field structure includes a null point at a height of 220 Mm. Being located very high in the corona, this region is not a subject of this study. Of greater significance is the region between $x = -500$ Mm and $x = -100$ Mm, at heights below 100 Mm, where the magnetic field cancels out. This can be considered representative of the quiet Sun corona. This setup, therefore, provides an opportunity to study the propagation of coronal waves through a highly non-uniformly magnetized corona. Figure 2 shows the Alfvén and sound speeds along the horizontal direction at $y = 10$ Mm and the vertical direction at $x = 0$ Mm. Along the horizontal direction, the Alfvén speed decreases from 1855 km s^{-1} to 387 km s^{-1} at $x = -100$ Mm (top panel of Fig. 2). Further away from the eruption, the Alfvén speed becomes lower than the sound speed, $c_s = 150$ km s^{-1}. Around $x = -500$ Mm, the Alfvén speed increases again due to the presence of the dipolar magnetic field, reaching 629 km s^{-1} at $x = -600$ Mm, $y = 10$ Mm. The bottom panel of Fig. 2 shows a more gradual reduction of the Alfvén speed along the vertical direction as the background quadrupolar magnetic field strength drops.

We use zero-gradient boundary conditions for all the variables at the left and right boundaries. This ensures that waves and shock fronts can pass through with minimal reflections, as we use approximate Riemann solver-based discretizations. At the bottom, the density and pressure are fixed according to their initial values. The magnetic field is set according to second-order zero-gradient extrapolation. The region of the added dipole field will first be subjected to controlled field deformations, generating a flux rope with an embedded prominence inside. This field deformation happens through spatiotemporally prescribed velocities enforced in the local ghost cell regions at the bottom boundary. The velocities at the bottom ensure the converging and shearing motions (V_x and V_z), while antisymmetry is applied for V_y. The converging flow V_x profile is defined following Eq. 5 in Liakh et al. (2020) assuming the center of the profile at $x_c = -600$ Mm, size parameters of the converging region is $W = 2\sigma$, $\sigma = 21.6$ Mm. The shearing velocity is defined as $V_z = -V_x$. The temporal evolution of these imposed bottom boundary flows is defined by Eqs. 15-17 in Jenkins & Keppens (2021) but with a smooth profile in time for the deactivation stage. The activation and deactivation times are chosen at 0 and 25 minutes, respectively. After the formation of the flux rope, a zero-velocity boundary condition is applied.At the top boundary, the density, pressure, and velocity components are set to match the corresponding values from the last computational cell within the physical domain. The magnetic field components are assigned values from the last cell of the physical domain but with the reverse sign.

In this study, the prominence is formed by artificially loading plasma into the flux rope dips using a source term in the continuity equation, following the approach adopted in previous studies (e.g., Liakh et al. 2020, 2021, 2023). The prominence, with a size of 4×4 Mm and a density of $\rho \approx 10^{-12}$ g cm^{-3}, is loaded at $x = -600$, $y = 10$ Mm during the time from 25 to 26.7 minutes. This method was chosen over a more realistic model of prominence formation (e.g., levitation-condensation) due to the time constraint associated with the perturbations from the eruption reaching the prominence region.

3. Results

The numerical experiment presented in this paper involves a large coronal region permeated by a complex magnetic structure. Animation 1 associated with Fig. 1 shows that within this region, several important processes occur, including a large-scale eruptive event with an associated extended current sheet underneath, the fragmentation of this current sheet into plasmoids, the propagation of perturbations over large distances, and the interaction of these perturbations with a remote prominence. Studying these regions individually helps to understand the global evolution.

3.1. *Eruption evolution*

The EFR becomes unstable immediately since we chose the catastrophe parameters accordingly. In the top row of Fig. 3, the EFR has already risen, and the front has formed in response to the initial force imbalance. The front is not perfectly circular due to variations in physical conditions, such as density, magnetic field, and consequently, the Alfvén and sound speeds in the vertical and horizontal directions (Fig. 2). We will explore this aspect in Section 3.2. The top row also shows the magnetic reconnection beginning below the EFR. As a result, the reconnection outflow interacts with the EFR, appearing as propagating density and temperature perturbation in the lower part of the flux rope. In Animation 2, this perturbation moves along the circular field lines (also visible in the middle row of Fig. 3).

The middle row of Fig. 3 shows that the EFR has reached a height of 200 Mm at 12.9 minutes. By this time, the front has

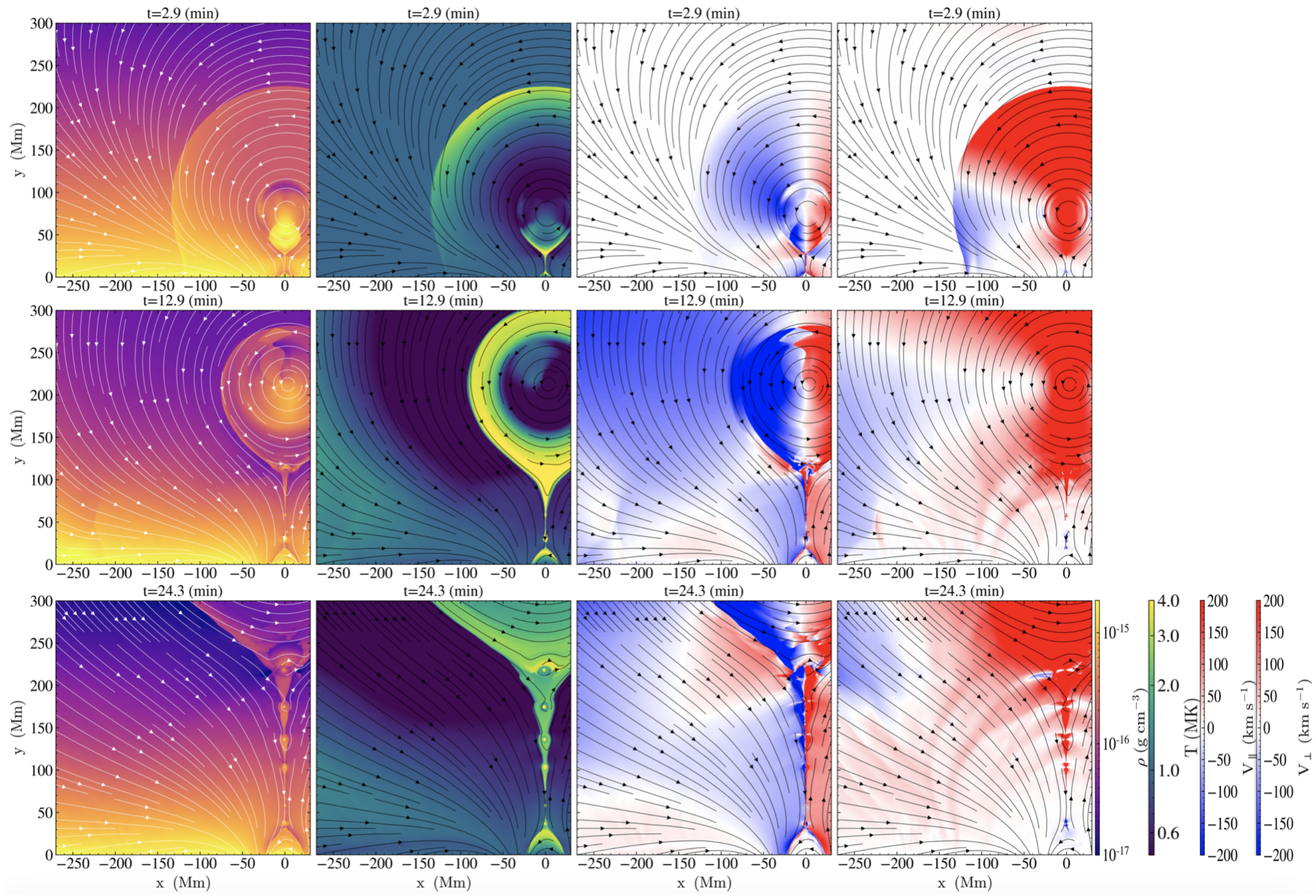

Fig. 3: Density, temperature, $v_{\parallel}$, and $v_{\perp}$ distributions during various stages of the eruption: onset (top row), the appearance of the secondary front and fragmentation of the current sheet (middle row), and multiple plasmoid formation in the current sheet (bottom row). Animation 2 shows the temporal evolution up to 57.2 minutes. (An animation of this figure is available online.)

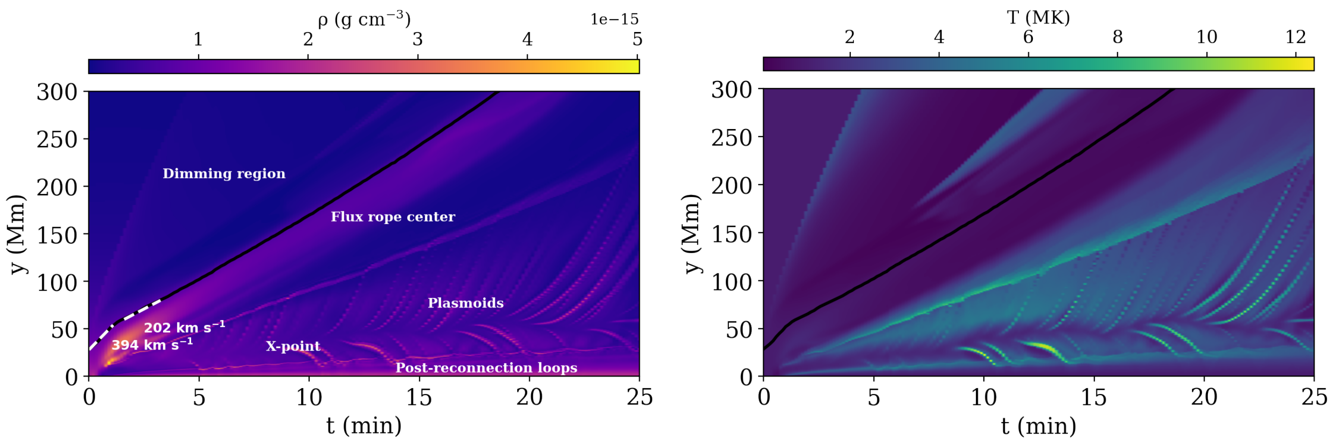

Fig. 4: Time-distance diagrams of density (left) and temperature (right) along the vertical cut at $x = 0$ Mm. The black line indicates the instantaneous center of the EFR.

propagated away from the considered region. Two other fronts remain seen in the longitudinal and transverse velocity distributions around the region from $x = -250$ to $x = -200$ Mm. These two fronts are remnants of the evolution of the main front. We will study these fronts in more detail in Section 3.2. In the same row, we observe a region of decreased density and temperature, which separates the eruption bubble from the surrounding corona. Due to its low density, this region appears dark in observations and is referred to as the dimming region (see, e. g. Attrill et al. 2009; Dissauer et al. 2018a; Vanninathan et al. 2018; Dissauer et al. 2018b, 2019; Veronig et al. 2019; Ronca et al. 2024).

The current sheet below the EFR elongates and starts fragmenting soon after the initiation of the experiment (4.7 minutes). The lower panel of Fig. 3 shows the moment where multiple plasmoids form in the current sheet. These plasmoids show increased density and temperature compared to the surrounding

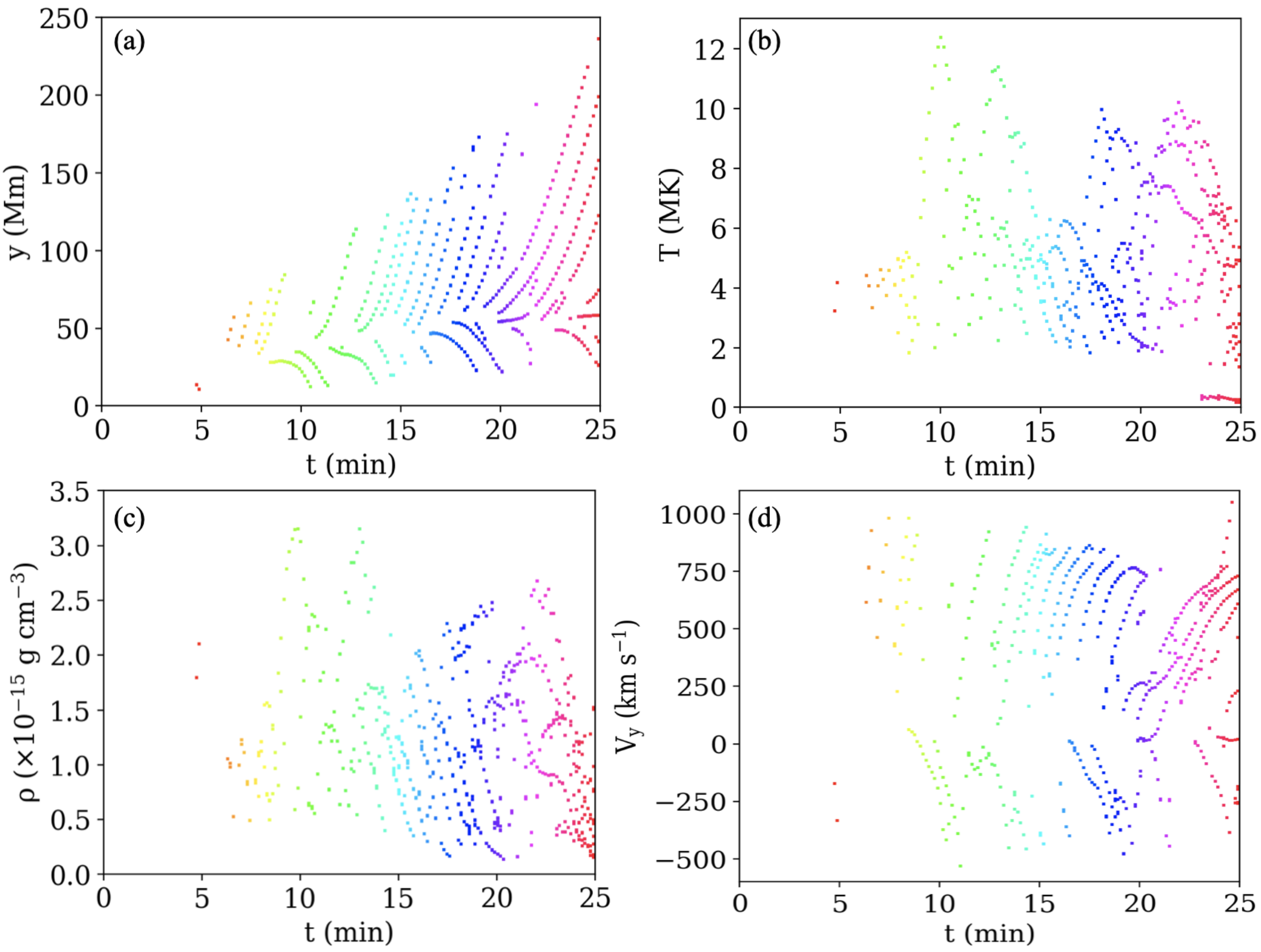

Fig. 5: Temporal evolution of plasmoids and their physical properties. Panel (a): plasmoid trajectories within the current sheet. Panel (b)-(d): temperature, density, and the vertical velocity v_y, corresponding to the instantaneous plasmoid positions. The same color scheme identifies the plasmoids across panels.

corona. The transverse velocity reveals multiple fronts associated with the motions of the plasmoids. The accompanying Animation 2 shows that plasmoid formation continues until the final stage of the experiment. As the EFR deviates from the strictly vertical direction after 30 minutes due to the asymmetry of the magnetic field, the current sheet also inclines to the left.

To understand the temporal evolution of the EFR, primary front, and current sheet along the vertical direction, we obtained time-distance diagrams of the density and temperature at $x = 0$ Mm (Fig. 4). Based on the slope of the black line, the initial velocity of the EFR is approximately 394 km s^{-1}. The initial acceleration of the EFR is due to the non-equilibrium caused by an excess of Lorentz force. After this stage, the EFR decelerates and rises at a lower speed of 202 km s^{-1}. The density perturbations, caused by the reconnection outflow interacting with the EFR, propagate along the circular field lines on both sides of the EFR. When they meet, they produce a plasma compression evident at the upper part of the EFR at $y = 170$ Mm from $t = 7.5$ minutes. As the experiment begins, the primary front rapidly moves away from the eruption. A dimming region between the front and the upper part of the EFR can be observed in the temperature time-distance diagram and slightly less pronounced in the density. As mentioned before, beneath the EFR, a current sheet forms, eventually breaking into plasmoids. From the location of the reconnection point in the time-distance diagrams, we note that fewer plasmoids emerge below the reconnection point than above. Those that emerge below the reconnection point merge with the post-reconnection loops underneath, while the ones above merge with the EFR.

To define and track the location of the plasmoids over time, we use a criterion based on the horizontal and vertical components of the magnetic field, namely where B_x and B_y simultaneously change sign. The plasmoid trajectories are depicted in panel (a) of Fig. 5. The other panels show temperature, density, and the vertical velocity, v_y. The colors represent the temporal evolution, allowing us to identify the plasmoids simultaneously present in the current sheet and their corresponding characteristics. The first plasmoid, marked with red color, forms in the current sheet at 4.7 minutes and moves downward. The maximum velocity is around 300 km s^{-1}, and the temperature exceeds 4 MK. From time $t = 6$ minutes, the plasmoid formation becomes more frequent. A chain of plasmoids is formed between 6 and 8 minutes (orange and yellow colors). They move upward, reaching very high velocities $\approx$ 1000 km s^{-1}. These plasmoids have an initial temperature above 4 MK but then are slightly cooling down. They have a relatively low density around 10^{-15} g cm^{-3}, which also slightly decreases as they move upward. Between 8 and 14 minutes, the plasmoids denoted by the light green color are formed both below and above the reconnection point. Those of them moving downward have velocity exceeding 500 km s^{-1} and contain very hot (12 MK) and relatively dense (3.2×10^{-15} g cm^{-3}) plasma compared to the surrounding corona. A second bunch of hot and dense plasmoids with characteristics 10 MK and 2.5×10^{-15} g cm^{-3} happens in the time interval 17.5 − 25 minutes (from dark-blue to pink colors).

Overall, the plasmoids in our numerical experiment appear to contain and transport upward and downward hot and dense plasma having substantial velocities. Most of the plasmoids form above the reconnection point and propagate upward following the EFR. These plasmoids accelerate significantly in the current sheet before merging with the flux rope. The downward-moving plasmoids contain denser and hotter plasma in most cases.

3.2. Wave propagation

The EFR generates various perturbations propagating through the coronal medium permeated by a complex magnetic field. This section studies the types of perturbations produced and aspects of their evolution. To enhance comparability with observations of such events, we also use synthetic SDO/AIA images.

The velocity divergence reflects plasma compression, allowing us to detect the fronts produced by the EFR. In Fig. 6, the red and blue lines allow us to indicate where plasma-β is close to unity and where the sound speed is nearly equal to the Alfvén speed. These are critical transitions in the background environment where plasma changes from magnetically- to gas-dominated. In this experiment, the perturbations are generated in a magnetically-dominated region of the EFR, where $\beta << 1$, and then propagate into an area of weak magnetic field where gas pressure starts to exceed magnetic pressure ($\beta > 1$). As the front crosses these critical lines, non-linear effects, such as mode conversion, may occur (see, e.g., Chen et al. 2016). This is important for our study, as we aim to understand the potential of coronal waves to probe the magnetic field of the coronal medium. Additionally, a portion of the energy of the primary front can be converted into secondary fronts, thereby weakening the initial perturbation.

Figure 6(a) shows the onset of the eruption, with the EFR center reaching a height of approximately 50 Mm. At 1.4 min, the primary front extends horizontally to about $x = -80$ Mm, and its upper edge reaches $y = 150$ Mm. Figure 6(a) also reveals the presence of another front lagging from the primary front, with its lateral extent reaching $x = -40$ Mm, although it is less pronounced. Both fronts are indicated by arrows in the panel. Panel (b) depicts the moment when the primary front impacts the bottom boundary where the zero-velocity condition is applied, producing an echo. The echo is evident well before the front reaches the equipartition lines. Panels (c) and (d) show the further evolution of the primary front as it passes the $\beta \approx 1$ and $v_A \approx c_S$ lines, revealing the formation of a secondary front. According to Chen et al. (2016), a fast-to-slow mode conversion can occur as a front moves from a magnetically-dominated plasma to one where gas pressure prevails. To study this further, we analyze the time-averaged magnetic and acoustic wave fluxes defined by Bray & Loughhead (1974) as:

$$\mathbf{F_{ac}} = p_1 \mathbf{v_1}\,, \tag{1}$$

$$\mathbf{F_{mag}} = \frac{\mathbf{B_1} \times (\mathbf{v_1} \times \mathbf{B_0})}{4\pi}\,, \tag{2}$$

where $\mathbf{B_0}$ is the initial magnetic field, and $p_1 = p - p_0$ and $\mathbf{B_1} = \mathbf{B} - \mathbf{B_0}$ are perturbations of the pressure and magnetic field with respect to their initial values. In regions where the Alfvén speed exceeds the sound speed, the magnetic flux can detect a combination of the Alfvén and fast magnetoacoustic modes. The acoustic flux detects the slow magnetoacoustic mode. We selected an averaging time of 20 minutes, during which the primary front propagates through the region of interest shown in Fig. 7, and the secondary front has already formed. Averaging the fluxes over multiple wave periods (approximately 5 minutes each) allows us to capture the energy transfer dynamics and cumulative effects.

As shown in the top panel of Fig. 7, the magnetic flux is predominantly concentrated along the path of the flux rope and the upward propagation of the main front. In this same region, the acoustic flux is mainly distributed around a height of 150 Mm. This distribution may be due to the rising EFR, which contains plasma with significantly higher pressure than the surrounding environment. Notably, the bottom panel reveals another enhancement in the acoustic flux around the current location of the equipartition lines (indicated by the red and blue solid lines). All described above makes us conclude the secondary front observed in Fig. 3 is the slow magnetoacoustic wave formed when the primary front crosses the equipartition lines.

On the contrary, in the regions where the sound speed exceeds Alfvén speed, the acoustic flux indicates the propagation of the fast magnetoacoustic wave. The bottom panel of Fig. 7 shows the lateral propagation of the fast magnetoacoustic wave beyond the positions of the red and blue solid lines.

To improve comparability with real observations, we generated synthesized images using MPI-AMRVAC as described by Xia et al. (2014) in three AIA channels to cover different temperature ranges: 304 Å (primarily capturing temperatures around 0.08 MK), 193 Å (1.5 MK), 131 Å (primary temperature response: 10 MK and secondary: 0.4 MK). The eruption is seen in 131 Å channel mostly due to the flows and compressions produced by the interaction of the reconnection outflow with EFR. From Fig. 3, we know that the temperature of this flowing plasma inside the EFR varies in the range 0.6 − 4.0 MK. Therefore, the plasma inside the EFR becomes visible due to the secondary peak of the 131 Å channel. In the 131 Å channel, we can also observe post-reconnection loops and plasmoids with high temperatures of 10 MK.

The primary front appears bright in the 193 Å channel in Fig. 8, indicating the plasma temperature of around 1.5 MK. A secondary front is also identifiable at around $x = -200$ Mm, corresponding to the front in Figs. 3, 6 and 7. Additionally, multiple fainter fronts are produced by plasmoids in the region between $x = -200$ and -100 Mm. In the corresponding Animation 3, these fronts become less visible and are difficult to identify at distances around 400 Mm from the reconnection site. They, therefore, cannot affect the distant prominence. Animation 3 also shows the formation of the dimming region and bright compression region surrounding the EFR, most clearly seen at $t = 4.3$ minutes.

Finally, the 304 Å channel corresponds to lower temperatures around 0.08 MK. From Fig. 8 and the corresponding Animation 3, this channel also shows details such as the compressions inside the EFR, post-reconnection loops, and the primary and secondary fronts.

To analyze wave propagation in the vertical and horizontal directions, we obtained time-distance diagrams in the 193 Å channel: a vertical diagram at $x = 0$ and a horizontal diagram at $y = 10$ Mm, corresponding to the height of the prominence center set by the mass loading process explained in Sec-

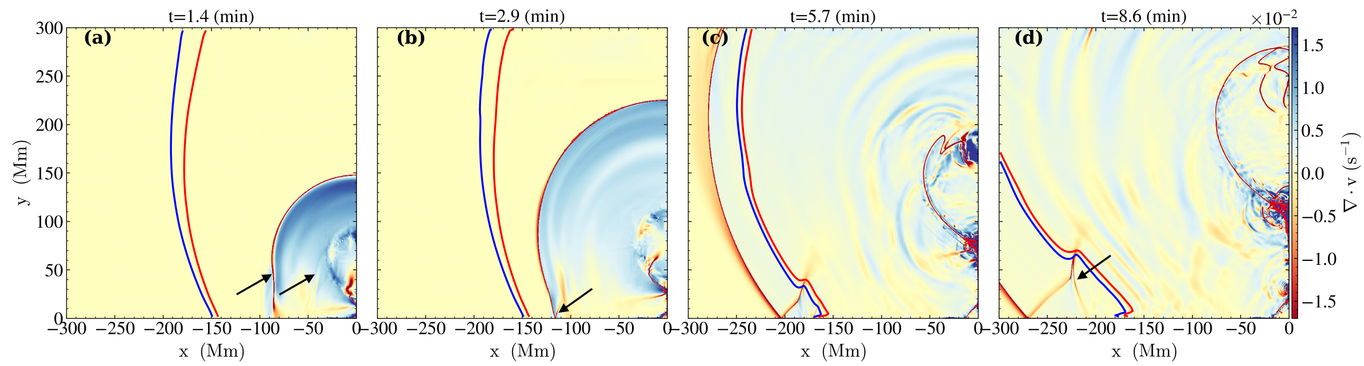

Fig. 6: Temporal evolution of $\nabla \cdot \mathbf{v}$. The red and blue contours represent $\beta \approx 1$ and $v_A \approx c_S$ ($\beta \approx 2/\gamma$), respectively. The arrows denote the main fronts detected during the onset of the eruption.

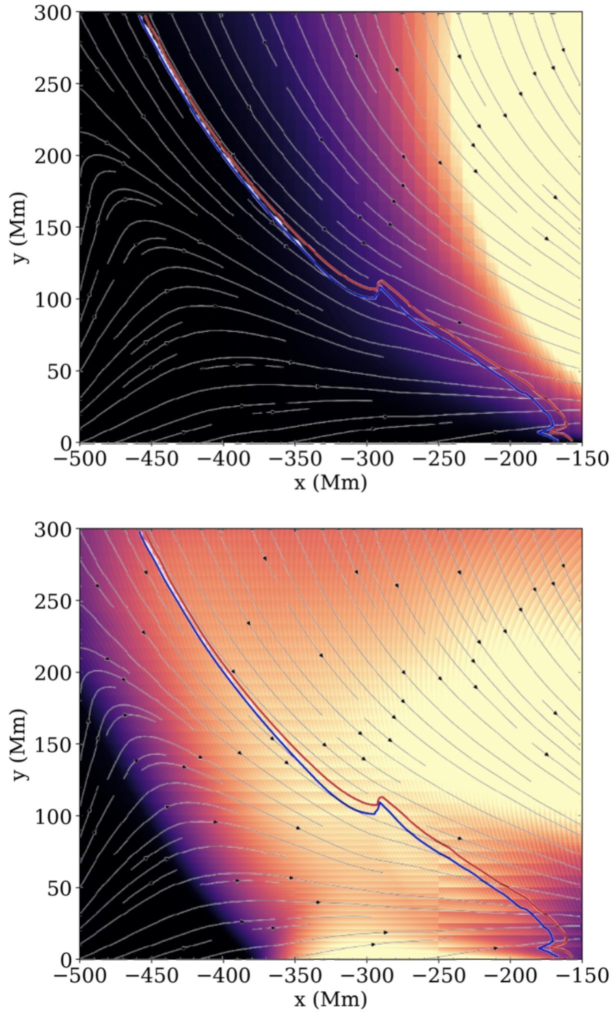

Fig. 7: Magnetic (top) and acoustic (bottom) fluxes on the left side of the reconnection site averaged over the first 20 minutes of the simulation. The grey lines denote the magnetic field lines at 20 minutes. Red and blue contours denote $\beta \approx 1$ and $v_A \approx c_S$ at $t = 20$ minutes.

tion 2. The left panel shows the vertical cut, highlighting similar features discussed in Fig. 4. In this time-distance diagram, the front produced by the eruption is identifiable. Estimating the slope velocities shows that the main front has an initial speed exceeding 1000 km s^{-1} but decelerates to 606 km s^{-1} as the magnetic field strength decreases. The grey line indicates the fast magnetoacoustic wave propagation at the local phase speed $v_{ph} = \sqrt{v_A^2 + c_s^2}$. The two slopes coincide, indicating that the front propagates upward as an ordinary fast magnetoacoustic wave.

The right panel illustrates wave propagation in the horizontal direction. The initial speed of the front exceeds 1000 km s^{-1}, but due to the rapid decrease in the magnetic field, the front quickly decelerates to 250 km s^{-1}. The grey line again shows the slope given by the local phase speed of the fast magnetoacoustic wave. Initially, the slopes coincide up to time 5 minutes. However, at a distance of 150 Mm, the front deviates from the grey line. This analysis suggests that the primary front initially propagates laterally as an ordinary fast magnetoacoustic wave and later becomes a shock wave.

At a distance of 600 Mm, the prominence region is located. The primary front reaches the prominence at approximately 30 minutes. As a result of the front interacting with the prominence region, a reflected front with a speed of 167 km s^{-1} is seen. Again, we compare the propagation of this reflected front to the fast magnetoacoustic mode and find an agreement. Additionally, a transmitted front forms with a slope velocity of $v = 83$ km s^{-1}, significantly slower than the primary front. We compare this front with the slow magnetoacoustic wave propagating at local sound speed in the region where $\beta << 1$. Initially, the slopes coincide, but later, this transmitted front slows down, appearing almost like a horizontal line and indicating a stationary front.

To this end, we have also analyzed the magnetic and acoustic fluxes, similar to Fig. 7, but centered around the prominence region and time-averaged throughout 20 – 40 minutes. In order to compute the fluxes using Eqs. 1, 2, the initial values of the pressure and magnetic field are assumed to be at 20 minutes. The top panel of Fig. 10 shows a bright region, indicating an increase in magnetic flux, which indicates propagation of fast magnetoacoustic and Alfvén waves in the magnetically-dominated region at the area of the prominence magnetic field. The bottom panel shows a bright front localized along the loops overlying the flux rope prominence region. This front is discussed previously regarding the right panel of Fig. 9. In the magnetically dominated region, the acoustic flux indicates the propagation of the slow magnetoacoustic wave. Everything described above leads us to conclude that this front is formed by the fast-to-slow mode conversion. It propagates along the loops, finally creating a stationary front.

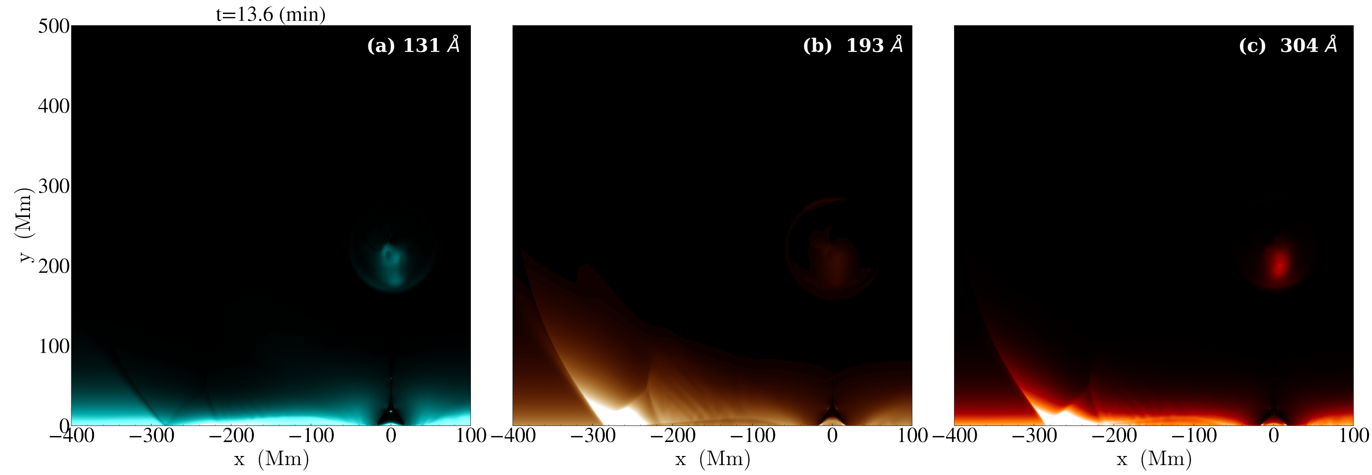

Fig. 8: Synthetic AIA channel images (131, 193, and 304 Å) of the eruption area at 13.6 minutes. The saturation levels for the fluxes in the 131, 193, and 304 Å channels are defined as follows: 1.5×10^{-8}, 3.0×10^{-7}, 8.0×10^{-9} DN s^{-1} pixel^{-1}, respectively. Note that these saturation levels are applied to all synthetic images presented in this paper. Animation 3 shows the temporal evolution up to 28.6 minutes. (An animation of this figure is available online.)

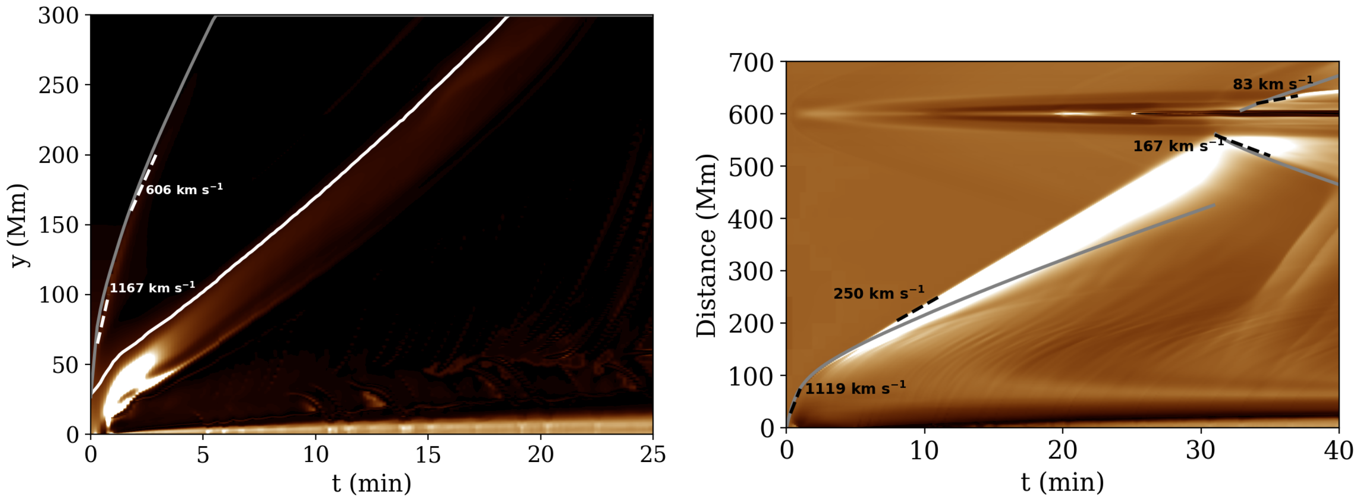

Fig. 9: Time-distance diagrams of 193 Å channel taken along the vertical cut at $x = 0$ Mm (left) and the horizontal cut $y = 10$ Mm (right). The vertical axis in the right panel corresponds to the distance from the eruption. The white solid line in the left panel denotes the instantaneous center of the EFR. Grey lines in both panels denote the propagation according to the local phase speed of fast and slow magnetoacoustic waves.

3.3. Prominence evolution

We have examined the evolution of the eruption, the resulting perturbations, and their propagation throughout the numerical domain. Another aim of this study is to understand how these eruption-driven perturbations interact with a distant prominence. In this section, we study the flux rope formation, the loading and evolution of the prominence mass within the flux rope, and the dynamic response of the prominence to the passing front. For this purpose, we analyze key parameters such as temperature, density, transverse and longitudinal velocities. Additionally, we study the appearance of the flux rope and prominence in synthetic images of 131, 193, and 304 Å channels.

Figure 11 and the corresponding Animation 4 depict the evolution around $x = -600$ Mm, from the formation of the flux rope and prominence to their late-stage evolution after passing of the primary front. The first row of Fig. 11 shows the moment when the flux rope is fully formed. At the center of the flux rope, there is a region of slightly higher density and lower temperature compared to its surroundings. This plasma originates from the lower corona and is lifted during the flux rope formation process. The prominence plasma, artificially loaded into the flux rope, appears as a dense and cold plasma block. The longitudinal velocity indicates that the prominence plasma begins to be compressed toward the center of the magnetic dips. The second row of Fig. 11 shows that the prominence has a narrower shape and larger density due to compression. Additionally, the formation of a 'tail' at the top part of the prominence is seen. This tail extends along the circular field lines toward the flux rope center. The density distribution shows that lifted plasma remains mainly close to the flux rope center. The longitudinal velocity suggests plasma continues flowing towards the main prominence body along the magnetic field. At this stage, the front from the eruption reaches the flux rope region, as shown by the transverse velocity and also indicated by the arrow in the last panel of the second row in Fig. 11. The interaction of the wave with the prominence is evident in Animation 4, associated with Fig. 11 and Animation 1, associated with Fig. 1. From Animation 1, the bottom part of the front

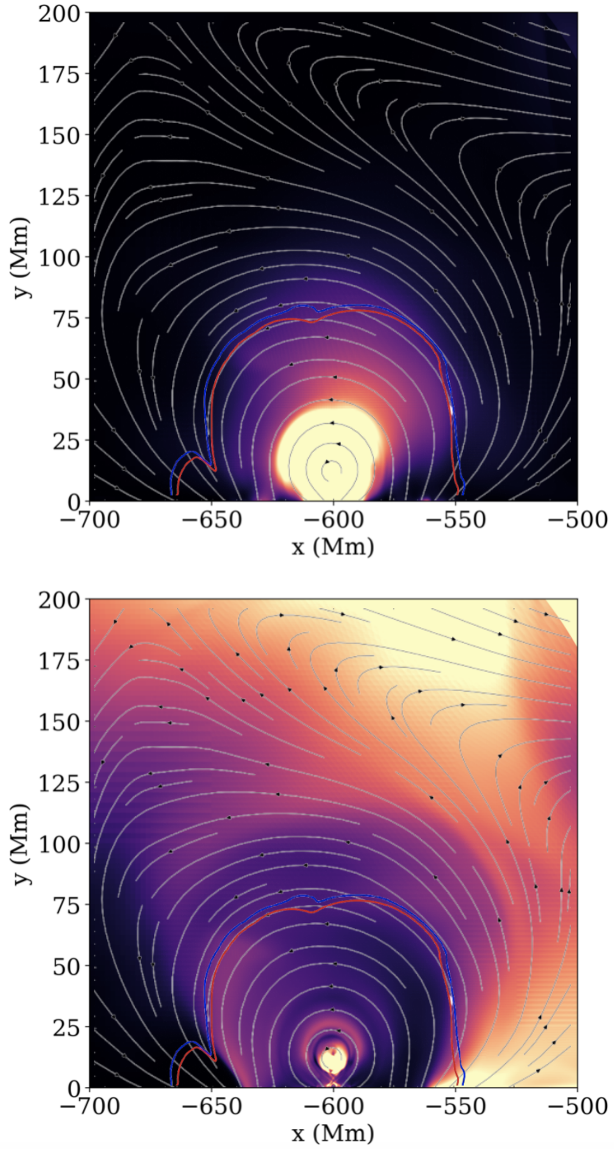

Fig. 10: Magnetic (top) and acoustic (bottom) fluxes around the prominence region, averaged over time 20 – 40 minutes of the simulation. The grey lines depict the magnetic field lines at t = 40 minutes. Red and blue contours denote $\beta \approx 1$ and $v_A \approx c_S$ at t = 40 minutes (solid line).

becomes oblique. This happens because the density decreases more rapidly than the magnetic field along the vertical direction between $x = -500$ and -100 Mm. This causes an increase in the Alfvén speed with height, leading to the inclination of the front.

From Animation 4, the flux rope and prominence are displaced to the left and down during the primary front propagation. As a result, the prominence starts to move around the center of the magnetic dips. Additionally, when the flux rope is pushed down, we can see a gradual disappearance of the post-reconnection loops below the flux rope. Figure 12 shows the details of the evolution of the current density and the magnetic field in the null point region. In order to follow the evolution of the same magnetic field lines each time moment, we start the integration at the bottom, where the zero-velocity condition is applied. Panel (a) shows the small vertical current sheet below the prominence just before the arrival of the primary front. When the front pushes the flux rope down, the current density of the vertical sheet starts to decrease (Fig. 11b). Panel (c) shows the moment the vertical current sheet entirely disappears. Finally, in panel (d), the formation of the horizontal current sheet is seen as the current density increases. The magnetic field lines of the post-reconnection loops reconnect at the horizontal current sheet and form the overlying magnetic field lines, which move gradually away from the reconnection region. The corresponding Animation 5 shows more details of the evolution of the null point, particularly that all the post-reconnection loops denoted in Fig. 12a are reformed by reconnecting with the field lines of the flux rope. McLaughlin & Hood (2004) highlighted the critical role of null points in the dissipation of fast magnetoacoustic waves, attributing this to increased Ohmic heating resulting from enhanced currents. Subsequent studies revealed that non-linear waves can deform null points, causing them to collapse into current sheets. This process leads to a sequence of horizontal and vertical current sheet formations, the process commonly referred to as oscillatory reconnection (McLaughlin et al. 2009, 2012). Oscillatory reconnection can be interpreted as damped harmonic oscillations. The results of our experiment resemble this behavior, as we observe rapidly attenuated oscillatory reconnection.

The third and fourth rows of Fig. 11 show the prominence evolution towards the end of the numerical experiment. The fourth row shows that prominence motions are almost entirely attenuated. The lifted plasma contained in the center of the flux rope is seen in a tiny region in the third row and entirely merges with the main prominence body in the fourth row. Another tail forms at the prominence bottom, and the longitudinal velocity shows that there is still plasma flowing towards the main prominence body from the edges of the flux rope.

Figure 13 quantifies the evolution of the total mass inside the flux rope after it is entirely formed (25 minutes). We define the instantaneous center of the flux rope as the maximum of the current density and identify the flux rope region with a local ellipsoid. Thus, every time moment, the center of this local ellipsoid dynamically evolves along the vertical direction at $x = -600$ Mm. The axes of the ellipsoid, which defines the shape of the magnetic field lines, are fixed to be 24.1 and 14.3 Mm in the vertical and horizontal directions, respectively. Then, we integrate the plasma density contained inside the flux rope, distinguishing between the coronal and the prominence plasma using threshold, $\rho_{crit} = 10^{-14}$ g cm^{-3}, respectively. Figure 13 shows the total mass of the coronal plasma is 4.6×10^3 g cm^{-1} at 25 minutes. The prominence plasma is gradually loaded during 1.67 minutes, marked by the two vertical grey lines. As this loaded plasma occupies the region initially filled with the coronal plasma, the total amount of coronal plasma shows a decrease. After the prominence is fully loaded, its total mass slowly increases, reaching $8{\times}10^3$ g cm^{-1} at the final stage of the experiment. Assuming that the length of the prominence in the third direction can be as long as 100 Mm, the total prominence mass is $\approx 10^{14}$ g, similar to that obtained in the recent 3D prominence simulation (Donné & Keppens 2024). Simultaneously, the coronal plasma decreases until reaching value 2×10^3 g cm^{-1}. The variation of the total masses reflects the accretion of the coronal plasma contained inside the flux rope towards the artificially loaded prominence. From this figure, we can see that the accretion rate is 3.7 g cm^{-1} s^{-1} and 2.1 g cm^{-1} s^{-1} before and after passing of the primary front. From this analysis, we do not see a strong influence of the primary front on the accretion rate inside the flux rope.

Fig. 14 and the associated Animation 6 show the brightening in all channels within the flux rope core, where the lifted plasma is localized. The flux rope formation leads to the depletion of the overlying loops. Therefore, the magnetic loops sur-

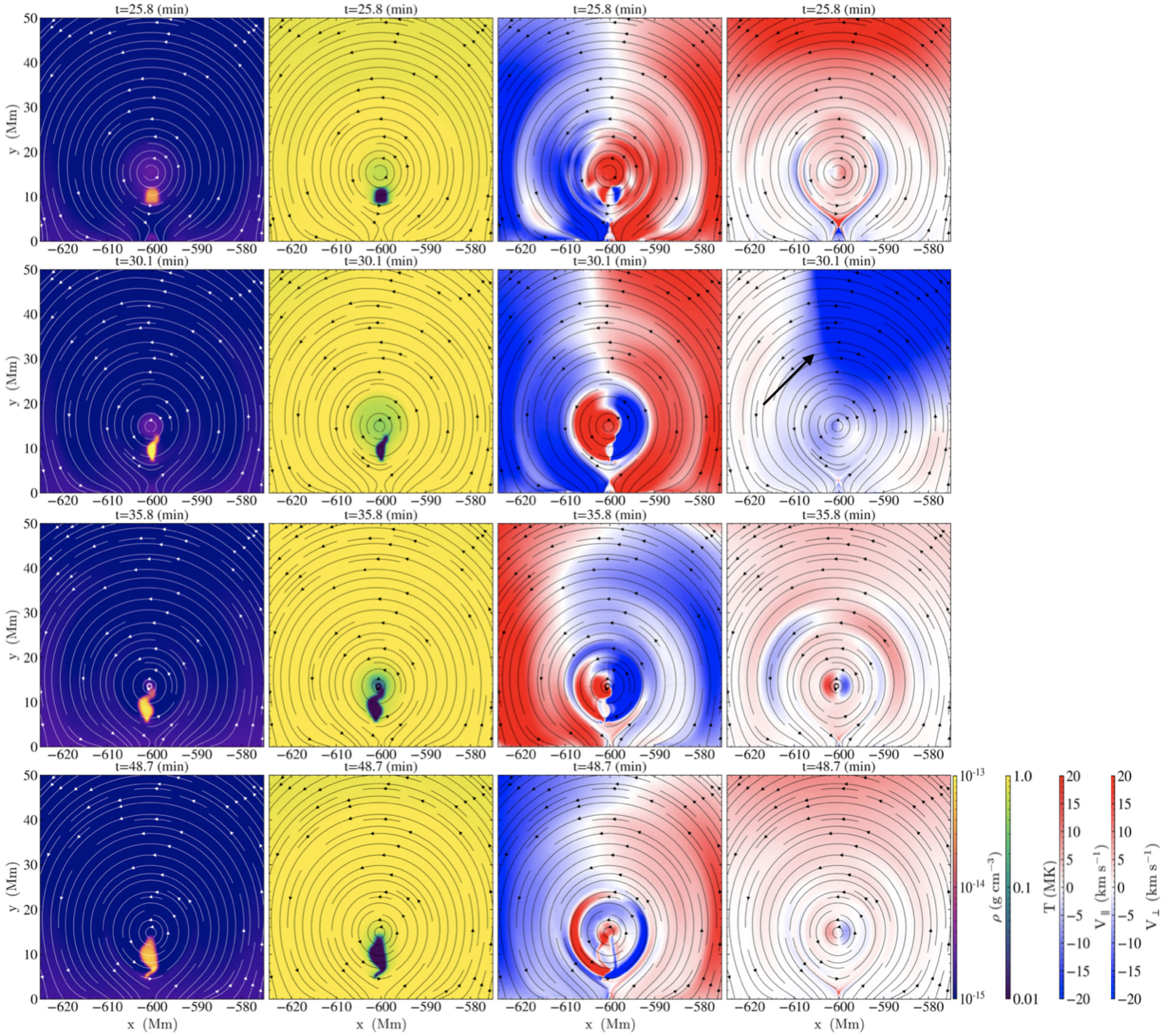

Fig. 11: Density, temperature, $v_{\parallel}$, and $v_{\perp}$ distributions during various stages of the experiment, focusing especially on the deformed dipolar region that hosts the prominence: prominence mass loading (first row), the wave interaction with the prominence (second row), prominence oscillations and mass accretion (third and fourth rows). The black arrow denotes the primary front. Animation 4 shows the temporal evolution up to 57.2 minutes. (An animation of this figure is available online.)

rounding the flux rope appear dark in all channels. The cold, prominence plasma loaded inside the flux rope appears dark, as the prominence plasma is optically thick in these channels. The prominence edges appear bright, reflecting the relatively hot and tenuous prominence-corona transition region (PCTR). The PCTR consists of plasma with temperatures spanning the range between prominence and coronal values, which explains its brightening in the 131, 193, and 304 Å channels. According to our chosen cooling curve, these temperatures correspond to the peak of the radiative cooling curve (see Fig. 1 in Hermans & Keppens (2021)). Given the relatively high density in the PCTR, this region is influenced by the significant radiative cooling, governed by the $\rho^2\Lambda(T)$ term. This cooling inevitably leads to a decrease in gas pressure within the PCTR, and to restore gas pressure balance, dense plasma contained within the flux rope begins to accrete onto the PCTR. Therefore, after the initial brightening inside the flux rope, visible in all channels, this brightening gradually fades, reflecting the plasma accretion onto the main prominence body. Depleting the flux rope leads to the forming of the dark coronal cavity in all AIA channels. The cavity grows as more plasma accretes on the main prominence body, and this process continues until the end of the numerical experiment.

Between 28 and 50 minutes, the passing of the EUV front is seen in the 193 Å channel (the white arrow in Fig. 14b). As the front passes, it interacts with the dark cavity and overlying loops. Notably, the primary front leaves behind a bright transmitted front that stops in the dark overlying loops. As previously discussed, this front forms due to fast-to-slow mode conversion. After the front passing, the prominence oscillates, a motion visible primarily due to the brightness of the PCTR. After a few minutes, these oscillations are attenuated. Additionally, the EUV

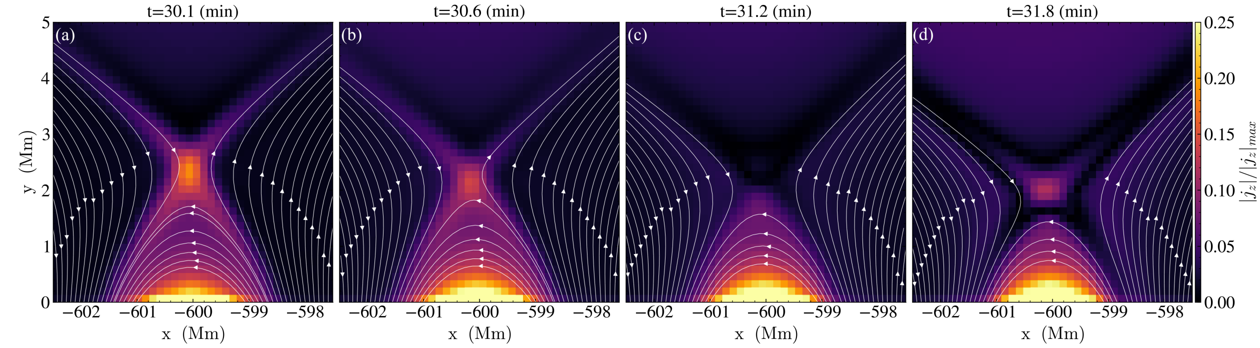

Fig. 12: Further zoomed details of the wave front interaction with the remote flux rope, this time focused on the X-point below the prominence hosting flux rope. Temporal evolution of the current density, $|j_z|$, normalized to the instantaneous maximum value in the shown region, $|j_z|_{max}$, along with the magnetic field lines at the bottom of the flux rope after its interaction with the primary front. The white lines in each panel denote the instantaneous position of the same magnetic field lines. Animation 5 shows the temporal evolution in the time interval 28.6 – 50.1 minutes. (An animation of this figure is available.)

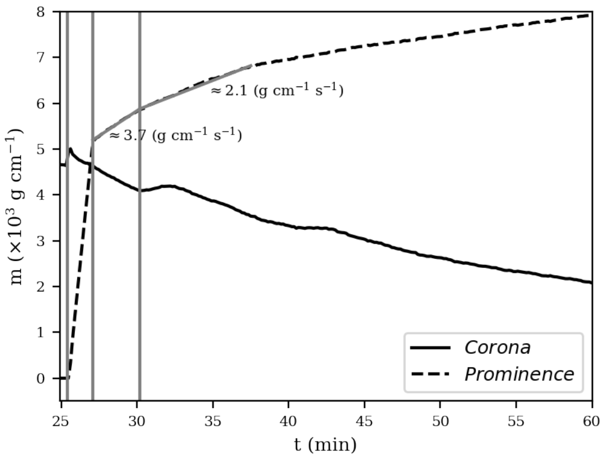

Fig. 13: Temporal evolution of the total mass of the coronal and prominence plasma using the threshold, $\rho = 10^{-14}$ g cm^{-3} in the dynamically evolving and tracked flux rope region. The vertical grey lines correspond to the activation and deactivation of mass loading and the arrival of the primary front.

front triggers magnetic reconnection discussed earlier, causing the bright post-reconnection loops to gradually disappear across all channels.

To investigate the interaction between the EUV front and the prominence, we generate time-distance diagrams for the 193 and 304 Å channels along the horizontal direction at $y = 10$ Mm (Fig. 15) and the vertical direction at $x = -600$ Mm (Fig. 16). Fig. 15 captures the flux rope formation during 0 – 25 minutes, showing the top part of the flux rope crossing $y = 10$ Mm, followed by the bright central region of the compressed and lifted plasma, and finally, the bottom part of the flux rope (i.e., the magnetic dips). Shortly after this, the mass-loading process begins and lasts about 1.67 minutes. The loaded plasma appears dark in both channels except for the PCTR. After the prominence is loaded, it undergoes a cycle of compression and rarefaction, which is disrupted by the arrival of the EUV front at around 30 minutes (see left panels in Fig. 15). Upon impact of the primary front, the prominence is displaced at around 3 – 4 Mm, and the oscillations are initiated. As plasma accretes onto the main prominence body, the region between 592 and 608 Mm becomes dark in both channels.

Figure 16 shows the evolution along the vertical cut. In the left panels, the primary EUV front passes the prominence region at 30 minutes. The right panels show zoomed views capturing the formation and rise of the flux rope. The brightening occurs due to plasma collected during flux rope formation. Later, this plasma is lifted by the flux rope, reaching heights of 10-20 Mm by $t = 25$ minutes. The prominence mass is loaded at 25 minutes and leads to a slight descent of the flux rope. The front arrives at 30 minutes, pushing the flux rope downward and initiating motions in the vertical direction. These motions attenuate entirely by time 45 minutes. The right panels also show bright plasma accreting onto the prominence plasma. This leads to the formation of the dark cavity above $y = 12 - 15$ Mm. The vertical size of the prominence increases significantly as a result of the mass accretion.

From the analysis described above, we conclude that the front from the eruption induces prominence plasma motion by displacing it to the left and simultaneously pushing it downward. To analyze local plasma motion, we could examine advection along magnetic field lines, similar to previous studies (see, e.g., Liakh et al. 2020). However, this method is not applicable when the magnetic field evolves significantly, as in this study. Therefore, we analyze longitudinal and transverse velocities interpolated along the trajectories of fluid elements, as performed in Liakh et al. (2023). We selected 20 fluid elements at $x = -600$ Mm and $y = 7.8 - 10.8$ Mm at $t = 29.6$ minutes, just after the prominence loading but before the perturbing front. The results of this analysis are shown in Fig. 17. The top panel shows the evolution of the longitudinal velocity. When the oscillations are established, their amplitudes vary with height $4.2 - 14.0\,\mathrm{km\,s^{-1}}$. We estimated the periods of these oscillations using the Lomb-Scargle periodogram. The period of these oscillations decreases with height, ranging from 15.1 to 12.4 minutes. Consequently, the top and bottom motions become unsynchronized by $t = 50$ minutes. We computed the time-averaged radii of curvature of the magnetic field lines for each fluid element, $R_c = 3.5 - 4.5$ Mm, in order to obtain the pendulum period, $P_{pendulum} = 2\pi\sqrt{R_c/g}$ defined by Luna & Karpen (2012), where g is the solar gravitational acceleration. The pendulum period also decreases with height from 13.4 to 11.9 minutes. We also estimate the attenuation time using the fitting of the longitudinal velocity with the damped sinusoid function. The attenuation time slightly decreases with height, ranging between 20 – 40 minutes.

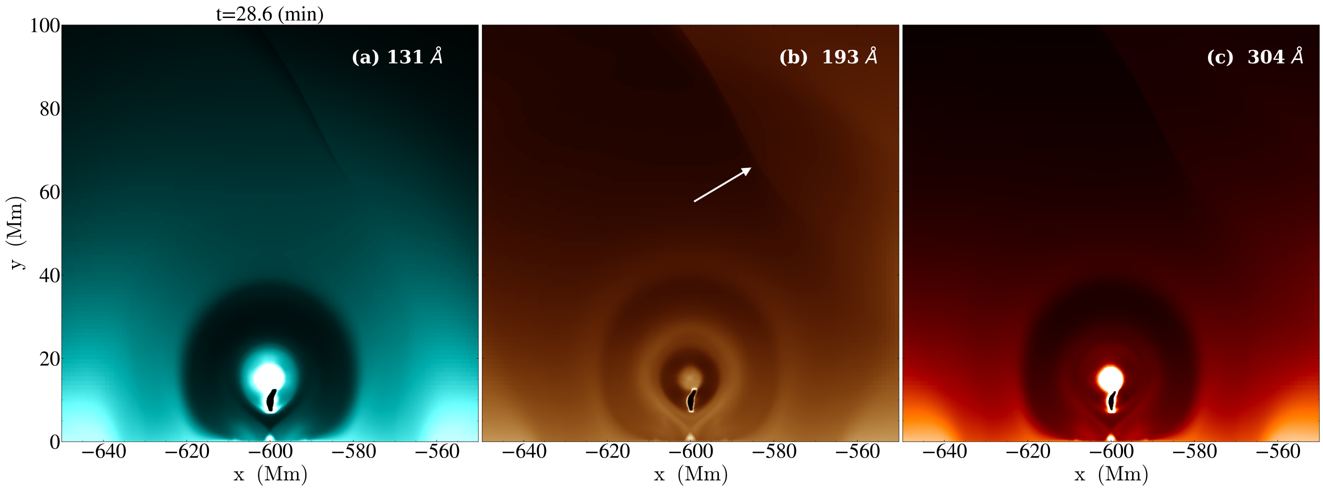

Fig. 14: Synthesized images of the prominence region in AIA channels 131, 171, and 193 Å, shown at 28.6 minutes. The white arrow denotes the primary front. Animation 6 shows the prominence formation, the passing of the primary front, and induced prominence dynamics up to 57.2 minutes. (An animation of this figure is available online.)

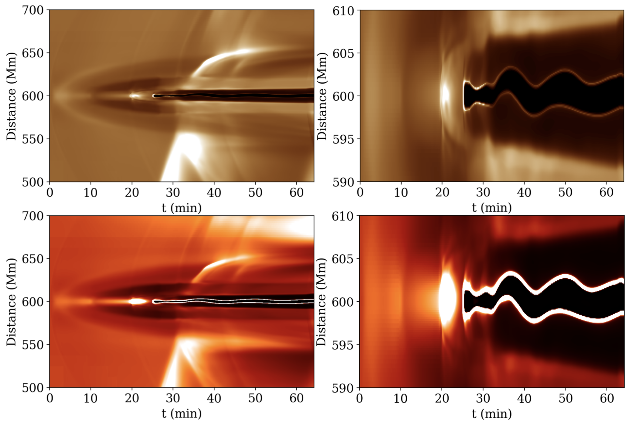

Fig. 15: Time-distance diagrams of the 193 Å (top) and 304 Å (bottom) SDO/AIA channels taken along the horizontal cut at $y = 10$ Mm. The right panels show a zoomed view around the prominence region. The vertical axes denote the distance from the eruption.

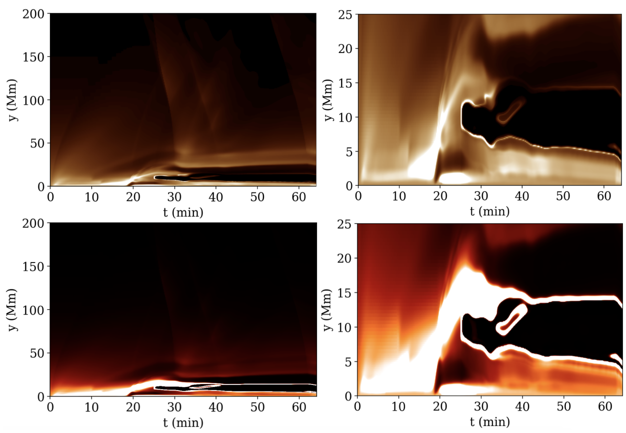

Fig. 16: Time-distance diagrams of the 193 Å (top) and 304 Å (bottom) SDO/AIA channels taken along the vertical cut at $x = -600$ Mm. The right panels show a zoomed view around the prominence region.

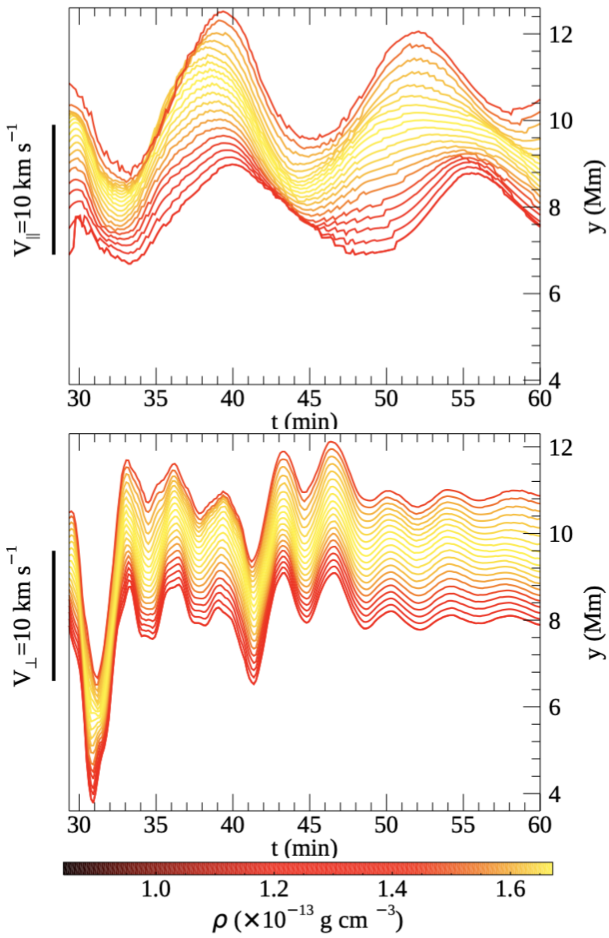

Fig. 17: Temporal evolution of $v_\parallel$ (top) and $v_\perp$ (bottom) obtained by tracking 20 fluid elements. The right vertical axis shows the initial height of the corresponding fluid element. The color bar corresponds to the initial density at the positions of the fluid elements.

The transverse velocity shows a more significant response to the front perturbation. When the flux rope is pushed downward, the initial transverse velocity is around $12.6 - 14.2\,\mathrm{km\,s^{-1}}$. These oscillations show more global character, having a constant period of $3.6 - 3.7$ minutes minutes at all heights. To interpret the period, we used the formula from Hyder (1966) for transverse oscillations in the case of a simple harmonic oscillator, where magnetic tension acts as the main restoring force: $P = \frac{2\pi\langle h\rangle}{\langle B\rangle}\sqrt{\pi\langle\rho_p\rangle} = 3.3$ minutes, where $\langle h\rangle = 8$ Mm, $\langle B\rangle = 13.4$ G, and $\langle\rho_{max}\rangle = 9\times10^{-14}$ g cm^{-3} are averaged prominence height, magnetic field strength, and maximum density, respectively, over the time interval of $30-60$ minutes. These oscillations are almost entirely attenuated at 40 minutes, and the attenuation time is estimated to be around 4 minutes.

4. Discussion

In this paper, we performed a 2.5D numerical experiment using the `MPI-AMRVAC 3.1` code to investigate the interaction between eruptive events and remote prominences. The model incorporates a 2.5D catastrophe magnetic field to generate the eruption and a dipole field to form the flux rope. This magnetic configuration allowed us to study the dynamics of an energetic eruption, the resulting perturbations, and the propagation of these disturbances through the non-uniformly magnetized solar corona. Exploring how coronal waves produced by an eruption interact with a distant flux rope prominence, we extend on our previous studies Liakh et al. (2020, 2023). Our main findings can be summarized as follows:

- The EFR becomes unstable immediately after the experiment begins, generating a quasicircular front. The EFR reaches approximately 100 Mm in height when the dimming region of reduced density and temperature separating the eruption bubble and surrounding corona becomes seen. Below the EFR, the current sheet forms, which eventually breaks into plasmoids. The plasmoids form both above and below the reconnection null point, transporting hot, dense plasma to the EFR and post-reconnection loops at significant velocities exceeding 1000 km s^{-1}. The downward-moving plasmoids contained extremely hot plasma inside, exceeding 12 MK.
- The EFR generates a front that propagates into the coronal medium, moving through regions with varying plasma-β conditions. Fast-to-slow mode conversion arises as this wave crosses the equipartition line, forming a secondary front. Synthesized SDO/AIA observations reveal that a fast EUV wave propagates in the vertical direction, initially reaching speeds above 1000 km s^{-1} and then decelerating to 600 km s^{-1} due to the decreasing magnetic field strength with height. The slope of the primary front coincides with the one given by the propagation of the ordinary fast magnetoacoustic wave. This front propagates horizontally, initially reaching speeds above 1000 km s^{-1} but then decelerating to 250 km s^{-1}. The front initially propagates as an ordinary fast magnetoacoustic wave but then transitions to a shock wave. A slow secondary EUV front emerges due to fast-to-slow mode conversion. Analysis of magnetic and acoustic fluxes shows evidence of the fast magnetoacoustic wave converting into the slow wave as it traverses the $\beta\approx1$ line. When the primary front reaches the prominence region, crossing from the high to low β region, it produces the reflected and transmitted EUV fronts.
- Once the flux rope is formed, we loaded the prominence plasma in the region of the magnetic dips. When the prominence is loaded, it is affected by the compression toward the center of the magnetic dips, becoming a denser and narrower structure. Converging flows are observed toward the tail at the prominence top. Over time, these flows become evident throughout the rest of the prominence body. This process depletes the flux rope, accreting plasma onto the prominence body.
- The wave interacts with the flux rope prominence, pushing it down and triggering magnetic reconnection between the flux rope and post-reconnection loops, causing the partial disappearance of these loops. Additionally, the wave inclines the flux rope prominence to the left, producing plasma motions along the magnetic field. The fluid elements analysis shows that the prominence oscillates both along the magnetic field and in the transverse directions. These two types of oscillations have different characteristic periods and attenuation times, indicating distinct restoring and attenuation mechanisms.

For the eruptive event, we used the setup from Takahashi et al. (2017), a 2.5D catastrophe scenario based on the force imbalance of the initial magnetic field. Despite the relative simplicity of this eruptive scenario, it successfully reproduces key features, including the shock front, dimming region, compression surrounding the dimming region, the current sheet beneath the EFR, plasmoids, and post-reconnection loops. Compared to Zhao & Keppens (2022), we increased the strength of the cylindrical current by increasing its radius and obtained a more intense front.

Perturbations below the EFR are initiated by the reconnection outflow interaction with the EFR. Takahashi et al. (2017) showed in similar configurations that dense, upward-moving flows create a high-density envelope inside the EFR. We find that this perturbation propagates along the lateral sides of the EFR and converges, forming a region of high-density plasma that highlights the EFR leading edge.

Ahead of the rising flux rope, the primary front is established. This front forms as a response to the initial force imbalance, generating the perturbation in density and temperature distributions. This approach to producing coronal waves has been used in multiple numerical studies (e.g., Wang et al. 2009; Mei et al. 2020). The front becomes quasicircular due to the anisotropic environment. Variations in magnetic field strength and plasma density along different directions influence how the perturbation propagates, probing the surrounding coronal environment (Liu et al. 2019; Downs et al. 2021).

A feature observed during the eruption is the formation of a dimming region characterized by reduced density and temperature, separating the expanding eruption from the surrounding corona. The decrease in plasma density and temperature within this region results in its dark appearance in synthetic and observational EUV images, as also reported by e.g., Attrill et al. (2009), Vanninathan et al. (2018), and Veronig et al. (2019), who identified similar dimming signatures associated with CMEs. In our synthetic images, the dimming region is surrounded by the compression layer, which is the most evident in the 193 Å channel, similar to the synthetic images shown in Downs et al. (2011).

As the EFR rises, an elongated current sheet forms below. It breaks into plasmoids early in the experiment. By detecting and tracking the plasmoids inside the current sheet, we obtained their properties. Our numerical experiment suggests that the upward-propagating plasmoids are accelerated up to substantial velocities, exceeding 1000 km s^{-1}. At the same time, the downward-moving plasmoids have extremely high-temperature values, around 12 MK, appearing bright in 131 Å synthetic images. Observations gave us estimates for the properties of plasma blobs, which are possible evidence of these plasmoids. Similarly, high velocities of plasma blobs have been detected by Liu (2013) in 131Å channel. More recently, plasma properties in these blobs have been estimated by Lu et al. (2022). The densities and velocities agree with our findings. Additionally, moderate plasma blob densities and temperatures have also been reported by Hou et al. (2024). Similarly, plasmoids with comparable properties were observed in our experiment. In contrast to the study by Zhao & Keppens (2022), we do not have plasmoids of chromospheric temperatures and densities, which originated from lifted and compressed chromospheric matter in the current sheet before it broke into plasmoids. The reason is that we do not include the lower atmosphere in our initial atmosphere, but this can be addressed in future studies.

In our numerical experiment, the eruption produced fast and slow fronts, which can be detected in the $\nabla \cdot \mathbf{v}$ distribution. Similarly, as in Mei et al. (2020), the fast front is evident, propagating far from the eruption, and the slow front is faint and hardly observed in synthetic images. Multiple fronts propagate away from the eruption and are associated with fast-moving plasmoids in the current sheet. The perturbations produced in this case are important for driving small-amplitude oscillations of nearby solar prominences, as we have shown in our recent study (Liakh et al. 2023). However, in the present case, these waves are fully attenuated before they can reach our distant prominence.

We studied the propagation of the primary front in the vertical directions. The speed of the vertical propagation of the perturbation very well agrees with the propagation of the fast magnetoacoustic wave, which decelerates propagating to a higher corona due to a decrease in the magnetic field strength. The synthetic 193 Å images show the fast EUV wave, which is an ordinary fast magnetoacoustic wave. The synthetic images also show the dark dimming region and bright compression layer due to the reconfiguration of the background coronal magnetic field due to the EFR rise. This agrees with results obtained in previous numerical studies (Chen et al. 2002, 2005; Cohen et al. 2009; Downs et al. 2011).

Studying the propagation of the fast front along the horizontal direction is of particular interest. This mimics the behavior of a CME-induced perturbation traveling across the solar disk and interacting with local non-uniformities in the magnetic field and plasma density. In our numerical experiment, the magnetic field configuration consists of three regions: the eruption, a smooth transition to the quiet Sun corona, and a transition to the prominence magnetic field. Our analysis reveals that initially, the fast front propagates as an ordinary fast magnetoacoustic wave. When it reaches the equipartition layer, it produces the secondary front. Further analyzing the properties of this front, we concluded that this is a slow magnetoacoustic wave similar to what has been obtained by Chen et al. (2016). The formation of the secondary front has been confirmed in observations in the region of significantly reduced magnetic field strength (Chandra et al. 2016). When the primary fast front moves even further into the region of the weak magnetic field, it becomes a fast magnetoacoustic shock wave since the local phase speed is significantly reduced. The EUV wave as a weakly shocked fast magnetoacoustic wave has also been confirmed in observations (Veronig et al. 2010; Takahashi et al. 2015; Long et al. 2015; Wang et al. 2020).

The primary front reaches the prominence region, producing a reflected front. The reflected fronts have been observed in the context of the interaction of EUV waves with different objects in the solar corona, such as coronal holes, loops systems, filaments (see, e.g., Long et al. 2008; Gopalswamy et al. 2009; Li et al. 2012; Shen & Liu 2012; Olmedo et al. 2012; Kienreich et al. 2013; Shen et al. 2013; Yan et al. 2013; Wang et al. 2020; Chandra et al. 2024). The primary front produces a slower transmitted front that propagates along the magnetic loops, decelerating there. The magnetic and acoustic fluxes analysis shows this is an ordinary slow magnetoacoustic wave. Moreover, the initial propagation speed agrees well with the sound speed. The most likely explanation is that we obtained this slow magnetoacoustic wave due to another fast-to-slow mode conversion. Our results agree with previous 3D simulations of the fast magnetoacoustic wave propagation from the gas-dominated region in the lower solar atmosphere to the magnetically-dominated atmosphere (Felipe et al. 2010). The conversion between fast and slow magnetoacoustic waves happens qualitatively in 3D, similar to what we see in two dimensions. The fast magnetoacoustic mode is transformed where $c_S = v_A$. After the transformation, a slow acoustic mode propagates along the field lines in the magnetically dominated region. The fast magnetic mode is reflected.

As mentioned before, the wave arrives at the prominence region with an oblique front due to the increase of the Alfvén speed with height. Our experiment shows that the front pushes the prominence down and to the left. This triggers prominence dynamics in the vertical direction and around the centers of the magnetic dips. In previous works (Liakh et al. 2020, 2023), we obtained similar results using an artificial perturbation that created an energetic wave, triggering simultaneously longitudinal and transverse oscillations. Observations also show the simultaneous driving of these different types of oscillations (Gilbert et al. 2008).

Analysis of the longitudinal and transverse velocities confirms that both oscillatory modes are excited. The transverse oscillations have a large initial amplitude that exceeds $14\,\mathrm{km\,s^{-1}}$, a constant period at different heights, and a very short damping time. The longitudinal oscillations have smaller initial amplitudes, periods that vary with height, and longer damping times. This means these two oscillations have different restoring forces and damping mechanisms. The constant period with height of the transverse oscillations suggests that this is a global normal mode, studied in many previous works (Terradas et al. 2013; Adrover-González & Terradas 2020; Liakh et al. 2020, 2023). As concluded in the earlier works, the main restoring force is the magnetic tension. The variation of the period of longitudinal oscillations with height can be explained by the pendulum model (Luna & Karpen 2012). In this model, the main restoring force of the longitudinal oscillations is the gravity projected along the magnetic field and the period defined only by the radius of the curvature of the corresponding field line. In the 2.5D flux rope, the radius of the curvature decreases with height, decreasing the corresponding period. This period difference can lead to the so-called zig-zag shape of the prominence (Luna et al. 2016). This is evident in the prominence evolution.

Significantly different damping times for these two types of oscillations suggest different mechanisms involved. For the transverse oscillations, wave leakage has primarily been considered as a damping mechanism (Zhang et al. 2019; Liakh et al. 2020, 2021). In our experiment, mass accretion, particularly the accumulation of material at the top of the prominence, may also play a role in damping. As the total plasma mass increases, the average momentum decreases, which can further dampen the oscillations. Notably, the effect of mass accretion on the damping of transverse oscillations has not been thoroughly studied either analytically or numerically.

Another possible explanation for the significant attenuation of the tranverse oscillations can be associated with the magnetic reconnection triggered by the arrival of the primary front. This front pushes the flux rope downward, compressing its field lines against those of the post-reconnection loops, inducing reconnection. This prevents the flux rope from returning to its original equilibrium height after the perturbation, causing it to remain lower. The current sheet shows an interesting evolution over this time. Initially, the vertical current sheet disappears, and the horizontal is formed instead due to the flux rope pushed down by the primary front. Over time, the current sheet realigns vertically again. Whether this process resembles oscillatory reconnection in the corona, as described by Karampelas et al. (2022), and whether it contributes to such significant attenuation remains an open question that is worth further investigation.

For the attenuation of the longitudinal oscillations, several mechanisms can play an important role, such as non-adiabatic effects (Zhang et al. 2019; Fan 2020), the energy transfer across the field lines (Liakh et al. 2021), mass accretion (Ruderman & Luna 2016), numerical dissipation (Liakh et al. 2020, 2021), or wave leakage (Zhang et al. 2019). In our experiment, we can observe the accretion of the plasma on the main prominence body. We estimated the damping time of the longitudinal oscillations using $\tau_D = 1.72 \cdot m(t = 0)/\dot{m} = 78.5$ minutes, where $m(t = 0)$ is the total prominence mass before perturbation, and $\dot{m}$ is the mass accretion rate (see Eq. 64 in Ruderman & Luna (2016)). This damping time greatly exceeds the one we got for these oscillations $20 - 40$ minutes. Considering all the abovementioned factors, the damping mechanism can not be explained only by plasma accretion. However, this damping mechanism is important in addition to non-adiabatic effects, energy transfer, wave leakage, and numerical dissipation.

Multiple recent observations confirm that triggering of prominence oscillations by EUV waves can originate from eruptions (Devi et al. 2022; Zhang et al. 2024a,b). For instance, Zhang et al. (2024a) observed one EUV wave with speed $835\,\mathrm{km\,s^{-1}}$ and another one decelerating from 788 to $603\,\mathrm{km\,s^{-1}}$. These waves induced prominence transverse oscillations that lasted only for a couple of periods and were the most evident in the 304 Å channel. The authors defined the main oscillatory characteristics period and damping time, $18 - 27$ minutes, and $33 - 108$ minutes, respectively. Devi et al. (2022) has also studied the EUV wave propagating with the speed $271\,\mathrm{km\,s^{-1}}$, which is very similar to the speed of the fast EUV wave in our experiment. The authors could detect the moment of interaction and pushing action of the EUV front on the prominence. After this interaction, the distant prominence showed transverse oscillations with periods in the range of $14 - 22$ minutes. Finally, Zhang et al. (2024b) investigated the transverse oscillations in the prominence and filament induced by the EUV wave and obtained periods of $29.5 - 31.1$ minutes, damping times of 44 and 21 minutes. Thus, our numerical experiment shows similar characteristics of the EUV waves and the induced prominences oscillations. We observed a slightly shorter period for the transverse oscillations compared to observations. This discrepancy is associated with the significantly smaller size of the simulated prominence relative to the observed ones. According to our analysis, the prominence size is a key parameter influencing the period of transverse oscillations. Therefore, incorporating larger prominences in our simulations would help reduce this difference.

5. Conclusions

In this study, we have investigated the interaction between eruptions and distant prominences through a 2.5D numerical experiment. Overall, this study provides a comprehensive view of the dynamics of coronal waves and prominence oscillations. We conclude that the fast EUV front produced by the eruption is a fast magnetoacoustic wave that evolves in the strongly non-uniform solar corona. This evolution leads to the formation of a secondary EUV front that can be interpreted as a slow magnetoacoustic wave. Additionally, when the fast EUV wave encounters the flux rope prominence, it produces the reflected and transmitted EUV fronts. Additionally, our numerical experiment and the corresponding synthetic images confirmed the formation of the dimming region and compression layer. Interaction between EUV waves and the remote prominence is evident, and it manifests in the prominence oscillations and triggering of the magnetic reconnection at the null point below the flux rope of the prominence. The amplitudes, periods, and damping times of these oscillations are in good agreement with previous numerical studies and observational results. However, our large-scale simulation is the first to combine these many facets in a single simulation that resolves details in all important regions, like the current sheet, near the null, or at the prominence location.

Our results show the importance of studying the interaction between eruptive waves and prominences. Future work could explore how different magnetic field configurations allow delayed eruptions or multiple fronts, such as in Hu et al. (2024). We could also allow a more realistic scenario of prominence formation, such as by levitation-condensation or evaporation-condensation, bringing in the chromospheric layers. Additionally, understanding the effects of mass accretion on prominence oscillations requires further investigation, which will be more evident in the case of the evaporation-condensation scenario. Using a delayed eruption setup allows sufficient time for the prominence to form, being located closer to the eruption region. This approach is particularly important for 3D simulations, as it enables a reduction in the size of the numerical domain, significantly lowering computational costs. While a large domain was feasible in our 2.5D simulations due to AMR, such an approach is computationally impractical in 3D. The extension of this experiment to 3D is crucial because it allows us to study different orientations of the flux rope prominence structure with respect to the perturbing front. Furthermore, the anchoring of the flux rope of the prominence provides an additional magnetic tension force that can significantly affect the triggering and properties of the transverse oscillations.

Acknowledgements. We acknowledge support by the ERC Advanced Grant PROMINENT from the European Research Council (ERC) under the European Union's Horizon 2020 research and innovation programme (grant agreement No. 833251 PROMINENT ERC-ADG 2018). RK acknowledges funding from FWO under grant agreement G0B9923N Helioskill, and under KU Leuven C1 project C16/24/010 UnderRadioSun.

References

Adrover-González, A. & Terradas, J. 2020, A&A, 633, A113
Afanasyev, A. N. & Zhukov, A. N. 2018, A&A, 614, A139
Arregui, I., Oliver, R., & Ballester, J. L. 2018, Liv. Rev. Sol. Phys., 15, 3
Asai, A., Ishii, T. T., Isobe, H., et al. 2012, ApJ, 745, L18
Attrill, G. D. R., Engell, A. J., Wills-Davey, M. J., Grigis, P., & Testa, P. 2009, ApJ, 704, 1296
Attrill, G. D. R., Harra, L. K., van Driel-Gesztelyi, L., Démoulin, P., & Wülser, J. P. 2007, Astron. Nachr., 328, 760
Biesecker, D. A., Myers, D. C., Thompson, B. J., Hammer, D. M., & Vourlidas, A. 2002, ApJ, 569, 1009
Bray, R. J. & Loughhead, R. E. 1974, The solar chromosphere
Brughmans, N., Jenkins, J. M., & Keppens, R. 2022, A&A, 668, A47
Chandra, R., Chen, P. F., & Devi, P. 2024, ApJ, 971, 53
Chandra, R., Chen, P. F., Fulara, A., Srivastava, A. K., & Uddin, W. 2016, ApJ, 822, 106
Chen, P. F. 2006, ApJ, 641, L153
Chen, P. F. 2011, Liv. Rev. Sol. Phys., 8, 1

Chen, P. F., Fang, C., Chandra, R., & Srivastava, A. K. 2016, Sol. Phys., 291, 3195
Chen, P. F., Fang, C., & Shibata, K. 2005, ApJ, 622, 1202
Chen, P. F., Wu, S. T., Shibata, K., & Fang, C. 2002, ApJ, 572, L99
Chen, P. F. & Wu, Y. 2011a, ApJ, 732, L20
Chen, P. F. & Wu, Y. 2011b, ApJ, 732, L20
Cohen, O., Attrill, G. D. R., Manchester, Ward B., I., & Wills-Davey, M. J. 2009, ApJ, 705, 587
Colgan, J., J. Abdallah, J., Sherrill, M. E., et al. 2008, ApJ, 689, 585
Delannée, C. & Aulanier, G. 1999, Sol. Phys., 190, 107
Delannée, C., Török, T., Aulanier, G., & Hochedez, J. F. 2008, Sol. Phys., 247, 123
Devi, P., Chandra, R., Joshi, R., et al. 2022, Adv. Space Res., 70, 1592
DeVore, C. R. & Antiochos, S. K. 2000, ApJ, 539, 954
Dissauer, K., Veronig, A. M., Temmer, M., & Podladchikova, T. 2019, ApJ, 874, 123
Dissauer, K., Veronig, A. M., Temmer, M., Podladchikova, T., & Vanninathan, K. 2018a, ApJ, 855, 137
Dissauer, K., Veronig, A. M., Temmer, M., Podladchikova, T., & Vanninathan, K. 2018b, ApJ, 863, 169
Donné, D. & Keppens, R. 2024, ApJ, 971, 90
Downs, C., Roussev, I. I., van der Holst, B., Lugaz, N., & Sokolov, I. V. 2012, ApJ, 750, 134
Downs, C., Roussev, I. I., van der Holst, B., et al. 2011, ApJ, 728, 2
Downs, C., Warmuth, A., Long, D. M., et al. 2021, ApJ, 911, 118
Fan, Y. 2020, ApJ, 898, 34
Felipe, T., Khomenko, E., & Collados, M. 2010, ApJ, 719, 357
Gilbert, H. R., Daou, A. G., Young, D., Tripathi, D., & Alexander, D. 2008, ApJ, 685, 629
Goedbloed, J. P., Keppens, R., & Poedts, S. 2019, Magnetohydrodynamics of Laboratory and Astrophysical Plasmas (Cambridge, UK: Cambridge University Press)
Gopalswamy, N., Yashiro, S., Temmer, M., et al. 2009, ApJ, 691, L123
Harten, A., Lax, P. D., & Leer, B. v. 1983, SIAM Rev., 25, 35
Hermans, J. & Keppens, R. 2021, A&A, 655, A36
Hou, Z., Tian, H., Madjarska, M. S., et al. 2024, A&A, 687, A190
Hu, J., Ye, J., Chen, Y., et al. 2024, ApJ, 962, 42
Hyder, C. L. 1966, ZAp, 63, 78
Jenkins, J. M. & Keppens, R. 2021, A&A, 646, A134
Karampelas, K., McLaughlin, J. A., Botha, G. J. J., & Régnier, S. 2022, ApJ, 925, 195
Keppens, R., Nool, M., Tóth, G., & Goedbloed, J. P. 2003, Comput. Phys. Commun., 153, 317
Keppens, R., Popescu Braileanu, B., Zhou, Y., et al. 2023, A&A, 673, A66
Keppens, R., Teunissen, J., Xia, C., & Porth, O. 2021, Comput. Math. Appl., 81, 316
Kienreich, I. W., Muhr, N., Veronig, A. M., et al. 2013, Sol. Phys., 286, 201
Li, T., Zhang, J., Yang, S., & Liu, W. 2012, ApJ, 746, 13
Liakh, V., Luna, M., & Khomenko, E. 2020, A&A, 637, A75
Liakh, V., Luna, M., & Khomenko, E. 2021, A&A, 654, A145
Liakh, V., Luna, M., & Khomenko, E. 2023, A&A, 673, A154
Liu, R. 2013, MNRAS, 434, 1309
Liu, R., Liu, C., Xu, Y., et al. 2013, ApJ, 773, 166
Liu, R., Wang, Y., Lee, J., & Shen, C. 2019, ApJ, 870, 15
Liu, W., Nitta, N. V., Schrijver, C. J., Title, A. M., & Tarbell, T. D. 2010, ApJ, 723, L53
Lohner, R. 1987, Comput. Methods Appl. Mech. Eng., 61, 323
Long, D. M., Baker, D., Williams, D. R., et al. 2015, ApJ, 799, 224
Long, D. M., Gallagher, P. T., McAteer, R. T. J., & Bloomfield, D. S. 2008, ApJ, 680, L81
Lu, L., Feng, L., Warmuth, A., et al. 2022, ApJ, 924, L7
Luna, M., Díaz, A. J., Oliver, R., Terradas, J., & Karpen, J. 2016, A&A, 593, A64
Luna, M. & Karpen, J. 2012, ApJ, 750, L1
Mazumder, R., Pant, V., Luna, M., & Banerjee, D. 2020, A&A, 633, A12
McLaughlin, J. A., De Moortel, I., Hood, A. W., & Brady, C. S. 2009, A&A, 493, 227
McLaughlin, J. A. & Hood, A. W. 2004, A&A, 420, 1129
McLaughlin, J. A., Thurgood, J. O., & MacTaggart, D. 2012, A&A, 548, A98
Mei, Z., Shen, C., Wu, N., et al. 2012, MNRAS, 425, 2824
Mei, Z. X., Keppens, R., Cai, Q. W., et al. 2020, MNRAS, 493, 4816
Meyer, C. D., Balsara, D. S., & Aslam, T. D. 2014, J. Comput. Phys., 257, 594
Moreton, G. E. & Ramsey, H. E. 1960, PASP, 72, 357
Moses, D., Clette, F., Delaboudinière, J. P., et al. 1997, Sol. Phys., 175, 571
Oliver, R. & Ballester, J. L. 2002, Sol. Phys., 206, 45
Olmedo, O., Vourlidas, A., Zhang, J., & Cheng, X. 2012, ApJ, 756, 143
Pant, V., Mazumder, R., Yuan, D., et al. 2016, Sol. Phys., 291, 3303
Piantschitsch, I., Terradas, J., Soubrie, E., et al. 2023, A&A, 679, A136
Piantschitsch, I., Terradas, J., Soubrie, E., et al. 2024, A&A, 687, A200
Piantschitsch, I., Vršnak, B., Hanslmeier, A., et al. 2017, ApJ, 850, 88
Porth, O., Xia, C., Hendrix, T., Moschou, S. P., & Keppens, R. 2014, ApJS, 214, 4
Ronca, G. M., Chikunova, G., Dissauer, K., Podladchikova, T., & Veronig, A. M. 2024, A&A, 691, A195
Ruderman, M. S. & Luna, M. 2016, A&A, 591, A131
Shen, Y., Ichimoto, K., Ishii, T. T., et al. 2014, ApJ, 786, 151
Shen, Y. & Liu, Y. 2012, ApJ, 754, 7
Shen, Y., Liu, Y., Su, J., et al. 2013, ApJ, 773, L33
Shen, Y., Liu, Y., Tian, Z., & Qu, Z. 2017, ApJ, 851, 101
Spitzer, L. 2006, Physics of Fully Ionized Gases, Dover Books on Physics (Dover Publications)
Takahashi, T., Asai, A., & Shibata, K. 2015, ApJ, 801, 37
Takahashi, T., Qiu, J., & Shibata, K. 2017, ApJ, 848, 102
Terradas, J., Soler, R., Díaz, A. J., Oliver, R., & Ballester, J. L. 2013, ApJ, 778, 49
Thompson, B. J., Plunkett, S. P., Gurman, J. B., et al. 1998, Geophys. Res. Lett., 25, 2465
Townsend, R. H. D. 2009, ApJS, 181, 391
van Leer, B. 1974, J. Comput. Phys., 14, 361
Vanninathan, K., Veronig, A. M., Dissauer, K., & Temmer, M. 2018, ApJ, 857, 62
Veronig, A. M., Gömöry, P., Dissauer, K., Temmer, M., & Vanninathan, K. 2019, ApJ, 879, 85
Veronig, A. M., Muhr, N., Kienreich, I. W., Temmer, M., & Vršnak, B. 2010, ApJ, 716, L57
Wang, B., Chen, Y., Fu, J., et al. 2016, ApJ, 827, L33
Wang, H., Liu, S., Gong, J., Wu, N., & Lin, J. 2015, ApJ, 805, 114
Wang, H., Shen, C., & Lin, J. 2009, ApJ, 700, 1716
Wang, J., Yan, X., Kong, D., et al. 2020, ApJ, 894, 30
Wang, Y.-M. 2000, ApJ, 543, L89
Wills-Davey, M. J., DeForest, C. E., & Stenflo, J. O. 2007, ApJ, 664, 556
Xia, C., Keppens, R., Antolin, P., & Porth, O. 2014, ApJ, 792, L38
Xia, C., Teunissen, J., Mellah, I. E., Chané, E., & Keppens, R. 2018, ApJS, 234, 30
Xue, Z. K., Yan, X. L., Qu, Z. Q., & Zhao, L. 2014, in ASP Conf. Ser., Vol. 489, Solar Polarization 7, ed. K. N. Nagendra, J. O. Stenflo, Z. Q. Qu, & M. Sampoorna, 53
Yan, X. L., Pan, G. M., Liu, J. H., et al. 2013, AJ, 145, 153
Yang, L., Zhang, J., Liu, W., Li, T., & Shen, Y. 2013, ApJ, 775, 39
Zhang, L. Y., Fang, C., & Chen, P. F. 2019, ApJ, 884, 74
Zhang, Q. M., Li, T., Zheng, R. S., Su, Y. N., & Ji, H. S. 2017, ApJ, 842, 27
Zhang, Q. M., Lin, M. S., Yan, X. L., et al. 2024a, MNRAS, 533, 3255
Zhang, Y., Zhang, Q., Song, D.-c., & Ji, H. 2024b, ApJ, 963, 140
Zhao, X. & Keppens, R. 2022, ApJ, 928, 45
Zheng, R. S., Jiang, Y. C., Yang, J. Y., et al. 2013, MNRAS, 431, 1359
Zhou, X., Shen, Y., Yuan, D., et al. 2024, Nat. Commun., 15, 3281
Zurbriggen, E., Cécere, M., Sieyra, M. V., et al. 2021, Sol. Phys., 296, 173